SUPER-Net: Trustworthy Medical Image Segmentation with Uncertainty Propagation in Encoder-Decoder Networks

Giuseppina Carannante, *Student Member, IEEE,* Dimah Dera, *Member, IEEE,*
Nidhal C. Bouaynaya, *Member, IEEE,* Hassan M. Fathallah-Shaykh, and Ghulam Rasool, *Member, IEEE.*

arXiv:2111.05978v3 [eess.IV] 21 Jan 2023

***Abstract*—Deep Learning (DL) holds great promise in reshaping the healthcare industry owning to its precision, efficiency, and objectivity. However, the brittleness of DL models to noisy and out-of-distribution inputs is ailing their deployment in the clinic. Most models produce point estimates without further information about model uncertainty or confidence. This paper introduces a new Bayesian DL framework for uncertainty quantification in segmentation neural networks: SUPER-Net: trustworthy medical image Segmentation with Uncertainty Propagation in Encoder-decodeR Networks. SUPER-Net analytically propagates — using Taylor series approximations — the first two moments (mean and covariance) of the posterior distribution of the model parameters across the nonlinear layers. In particular, SUPER-Net *simultaneously* learns the mean and covariance without expensive post-hoc Monte Carlo sampling or model ensembling. The output consists of two simultaneous maps: the segmented image and its pixelwise uncertainty map, which corresponds to the covariance matrix of the predictive distribution. We conduct an extensive evaluation of SUPER-Net on medical image segmentation of Magnetic Resonances Imaging and Computed Tomography scans under various noisy and adversarial conditions. Our experiments on multiple benchmark datasets demonstrate that SUPER-Net is more robust to noise and adversarial attacks than state-of-the-art segmentation models. Moreover, the uncertainty map of the proposed SUPER-Net associates low confidence (or equivalently high uncertainty) to patches in the test input images that are corrupted with noise, artifacts, or adversarial attacks. Perhaps more importantly, the model exhibits the ability of self-assessment of its segmentation decisions, notably when making erroneous predictions due to noise or adversarial examples.**

***Index Terms*—Bayesian deep learning, encoder-decoder networks, reliability, segmentation, trustworthiness, uncertainty estimation.**

I. Introduction

DRIVEN by the superior performance achieved in many areas, various deep learning (DL) models have been advanced to analyze medical data, e.g., radiological images and pathology slides. Several methods have achieved, if not surpassed, prognosis parity with specialized medical personnel [1]–[4]. However, their successful deployment in clinical settings remains limited. While several autonomous algorithms are doubtlessly employed for many everyday tasks — e.g., spam filters for emails or biometrics that unlock our cellphones —, there is less assertive willingness to utilize the same algorithms for risky, sensitive data, such as medical images.

The main challenge that hinders the widespread and effective use of DL in clinical settings is the lack of reliable and trustworthy predictions [5], [6]. For example, a system encountering unseen test examples, which lie outside of its training data distribution, could easily make unreasonable suggestions, and as a result, unjustifiably bias the human expert. The need for reliable models is further exacerbated owing to recent studies showing the vulnerability of DL models to adversarial inputs — perturbations that are imperceptible and would not mislead the decisions of a human observer but force a trained DL model to make erroneous predictions [7]. Some studies have demonstrated the vulnerability of medical models to adversarial perturbations [8], [9]. Consequently, DL in the field of medicine may be uniquely susceptible to adversarial attacks, both in terms of monetary incentives and technical vulnerability [9].

For the successful deployment of DL models in the real-world, e.g, a clinic, these models should provide information on the uncertainty or trustworthiness of their predictions. The user of these models should be aware of the level of confidence in the models' predictions. Such information could be very useful when the DL model is essentially guessing at random due to excessive noise in the input or possible adversarial attacks. Unfortunately, as most DL models are inherently deterministic, a measure of confidence or uncertainty is not readily available at their output.

Estimating the confidence of a model requires a probabilistic interpretation of the model's parameters, i.e., treating model parameters as random variables endowed with a probability distribution. Through Bayesian inference, the posterior distribution of the model parameters can be found. At test time, the second moment, i.e., the covariance, of the predictive distribution can serve as a measure of confidence or uncertainty in the predicted output. Several Bayesian models have been developed for the classification and regression problems [10]–[16]. Trade-offs between prediction accuracy, confidence estimation, and scalability are at the heart of these different approaches [17]. Recently, Dera *et al.* proposed a variational moments'

G. Carannnate, and N. C. Bouaynaya are with the Department of Electrical and Computer Engineering, Rowan University, Glassboro, NJ, 08028 USA (email: carannang1@rowan.edu, bouaynaya@rowan.eduand rasool@rowan.edu.)

D. Dera is with the Department of Electrical and Computer Engineering, University of Texas Rio Grande Valley, TX, 78520 USA (email: dimah.dera@utrgv.edu).

G. Rasool is with the Machine Learning Department, Moffit Cancer Center, Tampa, FL 33612 USA (email: ghulam.rasool@moffitt.org).

H. M. Fathallah-Shaykh is with the Department of of Neurology, University of Alabama at Birmingham School of Medicine, Birmingham, AL 35294-1170 USA (email: hfshaykh@uabmc.edu).

propagation (VMP) framework that provides a meaningful and scalable framework for uncertainty propagation and estimation in deep neural network (DNN) classifiers [14].

A relatively less amount of work focuses on quantifying uncertainty in pixel-level segmentation tasks using Bayesian DL models. The challenge in learning uncertainty for each pixel arises from propagating high-dimensional posterior distributions of the model's parameters through multiple stages of non-linearities in the encoder-decoder architecture. Furthermore, the model must provide an *instantaneous* uncertainty map at test time, i.e., simultaneously output the prediction (the segmentation) and corresponding pixel-level uncertainty map *without* resorting to expensive Monte Carlo sampling techniques or model averaging (ensemble).

Previous work focused solely on uncertainty quantification in classification neural network models, notably Convolution Neural Networks (CNNs) [14]. The mathematical derivations presented in [14] are not sufficient for uncertainty propagation in encode-decoder-based segmentation neural networks. The challenges in adopting the VMP framework in segmentation lie in the nature of the learning task: semantic segmentation requires the extraction of both global and local contextual information by encoding then decoding the input data. Consequently, segmentation networks are fundamentally different than classification networks, e.g., CNNs. The mathematical derivations for the decoder part were never presented previously and the flow of uncertainty from the encoder to the decoder was never considered within an analytical and systematic framework. The decoder presents specific non-linearities and operations, e.g., up-sampling, padding, and concatenation, that require new mathematical derivations to track the propagation of the uncertainty. In addition, our previous work estimated a scalar (or a vector) value of variance that is associated with the predicted class [14]. This work introduces the notion of dense, pixel-level uncertainty map that is provided simultaneously along with the predicted segmentation.

In this paper, we develop a VMP framework for segmentation tasks, SUPER-Net, and extensively evaluate it for various medical imaging datasets under various noisy and adversarial conditions. By leveraging key concepts from probability density tracking in nonlinear and non-Gaussian systems [18], [19], we propagate the first and the second moments of the posterior distribution of network parameters through the nonlinear layers of an encoder-decoder type segmentation architecture. The developed approach is tested using various medical segmentation datasets consisting of Magnetic Resonance Images (MRIs) and Computed Tomography (CT) scans. The proposed VMP formulation and the derived mathematical relationships presented in the paper are applicable to various DNN architectures.

The contributions of this paper are summarized as follows:

(1) Formalize a scalable Bayesian framework that *simultaneously* learns pixelwise prediction and confidence in encoder-decoder segmentation networks by analitically approximating and maximizing the evidence lower bound (ELBO). Using first-order Taylor series approximation, we derived closed-form expressions to propagate the first two moments (mean and covariance) of the posterior distribution of the model parameters given the training data and update them during backpropagation; thus, effectively learning the intrinsic uncertainty of the model. We derive mathematical relations for all operations involved, rendering a method that is adaptable to other models, e.g., Variational Autoencoders, and to other tasks as well.

(2) Develop a Bayesian DL architecture that instantaneously outputs two maps, (1) the segmented image, and (2) the uncertainty map of the predicted segmentation. These two maps are delivered simultaneously and *without* requiring any Monte Carlo sampling at inference time. That is, the generated uncertainty was intrinsically learned by the model rather than estimated post-training.

(3) Extensively evaluate the performance of the proposed SUPER-Net for various medical segmentation tasks and under various signal-to-noise ratios (SNRs) and conditions. A thorough robustness analysis is conducted by assessing the performance of the model and uncertainty map under these perturbations of the input data.

II. Related Work

Image segmentation is a fundamental problem in computer vision. Its application areas range from medical image analysis to scene understanding for autonomous vehicles. Several DL-based techniques have been proposed over the years to tackle pixel-level segmentation; a detailed review of all such methods is out of the scope of this paper and the reader is referred to a recent survey on the topic [20].

The success of CNNs in classification tasks has led researchers to extend these models for segmentation. In classification, the complete image is assigned a class label whereas in segmentation, each pixel in the image is classified into one of the classes. Fully Convolutional Networks (FCNs) represent a powerful class of CNNs that are trained end-to-end to perform pixel-wise predictions, called semantic segmentation. In FCNs, the standard CNN architecture (i.e., convolutional layers, downsampling and fully-connected layers) is modified by appending a decoder that converts the feature vector (encoded input) into a semantic segmention mask through up-convolutions, upsampling, and employing a pixel-wise loss function [21]–[27].

More recently, *encoder-decoder* architectures have gained popularity [28], [29]. The *encoder* path reduces the dimensionality of the input by extracting low-dimensional (salient) features of the data, while the *decoder* expands the encoded features to a map that has the same size as the input to perform pixel-wise classification. Several works have focused on modifying and fine-tuning the encoder-decoder architecture to improve segmentation, e.g., by introducing skip connections, dilated convolutions, wide contest blocks or compression extraction modules [28]–[32].

These architectural advances, however, focused on deterministic models that try to attain higher accuracy as the prime metric of model performance. Accuracy, no doubt, is an important metric but it does not convey the full picture. Reliability, robustness, and trustworthiness are important metrics for these models. An unreliable model is vulnerable and can jeopardize

the clinical system by exposing it to possible fraud, large monetary losses, technical vulnerabilities, lawsuits, and even loss of lives [9]. In the content of semantic segmentation, there are two main approaches to derive uncertainty estimates associated with segmented images: Monte Carlo (MC) dropout and model ensemble [33]–[46].

MC dropout is the most popular approach as it does not require major changes in the neural network architecture [10]. The uncertainty information is obtained, at inference time, from the sample variance of multiple MC forward passes through the network. Several researchers have applied this technique for various segmentation tasks [33]–[37]. For instance, a full-resolution residual network is used for brain segmentation in [37], while the QuickNAt architecture is used in [34]. A CNN-based network for lesion detection and vessel extraction was adopted in [35], [36].

In ensemble methods [47], after training multiple networks usually with random initialization, several segmentation estimates are produced, and their variation is used as a measure of confidence [38]–[41]. For example, [40] uses a ResUNet architecture with soft dice loss and two regularization terms to diversify the ensemble members. Authors in [38] generate diversity in the ensemble by considering predictions generated by different architectures and models.

The concept of generating several segmentation samples was leveraged in various ways, e.g., by combining hierarchical probabilistic models with variational autoencoders, by using data augmentation at test time, or using batch-normalization [42]–[44]. Authors in [45], [46] analyzed MC dropout and ensemble methods on clean datasets by evaluating some training settings, e.g., number of samples/models and different cost functions for segmentation. They concluded that – although both approaches result in uncertainty measures that show a relationship with segmentation quality - MC dropout is more convenient than ensembles as we are only required to train one model that allows sampling from it as often as desired. Some works combined the two approaches; for example, in [48] ensemble members are generated by changing the dropout rate.

However, all these approaches and methods estimate uncertainty post-training or at test/inference time. They adopt a frequentist approach where the uncertainty is computed at test time from the sample variance of multiple runs through the network or from multiple networks. In particular, the segmentation networks are not "trained" to learn uncertainty or variance as an intrinsic network parameter. The challenge stems from the mathematical propagation of the posterior distribution through the multiple (non)linear layers of a network. In addition, most studies considered only clean datasets and did not perform any noise analysis or consider adversarial attacks. In contrast, the proposed SUPER-Net framework learns the uncertainty during training and outputs simultaneously the predicted segmentation and its uncertainty map. A framework to learn the variance is proposed in [14], but derivations are limited to CNNs rendering the approach unsuitable for the more complex end-to-end segmentation tasks. Building upon this work, we develop a Bayesian framework that propagates the first and the second moment of the variational posterior distribution across all layers of a segmentation DL model. At test time, the uncertainty in the predicted segmentation decision is produced by the network as the covariance matrix of the predictive distribution simultaneously alongside the segmentation without resorting to multiple runs.

III. SUPER-Net: Segmentation with Uncertainty Propagation in Encoder-decodeR Networks

We derive a Bayesian framework where the first two moments of the posterior distribution are learnt simultaneously by (forward and backward) propagation through the network layers. For scalability and efficiency of the proposed approach, we adopt the Variational Inference (VI) technique; but rather than estimating the expected log-likelihood using expensive Monte Carlo sampling, we approximate its first two-moments with a first-order Taylor-series expansion. In the sequel, we present our mathematical results. An illustration of the SUPER-Net model is presented in Figure 1.

A. Mathematical Notations

Scalars are represented by lower-case letters, e.g., x, x_i. Vectors are represented by bold lower-case letters, e.g., $\mathbf{y}$. All vectors are column vectors. y_i denotes the i^{th} element of vector $\mathbf{y}$. Matrices are represented by bold upper-case letters, e.g., $\mathbf{A}$. $\text{Tr}(\cdot)$ denotes the trace of a matrix, i.e., the sum of its diagonal elements. ^{T} denotes the transpose operator, and $\text{vec}(\cdot)$ denotes the vectorization operator. The Hadamard product, i.e., the element-wise product, is denoted with $\odot$, while $\times$ represents matrix-matrix or matrix-vector product. Tensors with three or more dimensions are represented by curly bold upper-case letters, e.g., $\boldsymbol{\mathcal{X}}$. If x is a random variable, $\mathbb{E}[x]$ denotes the expected value of x. We use $\boldsymbol{\mathcal{W}}_e^{(k_c)}$ to represent the k_c^{th} convolutional kernel of the c^{th} layer. K_c denotes the total number of kernels in layer c. The subscripts e and d represent the encoder and decoder path operations, respectively.

B. Bayesian Deep Learning and Variational Inference

In Bayesian statistics, the unknown parameters are fully characterized by their posterior distribution given the observations. In Bayesian DL, the network parameters Ω are endowed with a prior probability distribution $p(\Omega)$ and all information about the parameters is embedded in the posterior distribution $p(\Omega|\mathcal{D})$ given the (training) data $\mathcal{D} = \{\boldsymbol{\mathcal{X}}^i, \mathbf{y}^i\}_{i=1}^N$. Once the posterior is estimated, the predictive distribution, i.e., the distribution of the test data, can be derived as:

$$p(\mathbf{y}^*|\boldsymbol{\mathcal{X}}^*, \mathcal{D}) = \int p(\mathbf{y}^*|\boldsymbol{\mathcal{X}}^*, \Omega)\ p(\Omega|\mathcal{D})\ d\Omega, \tag{1}$$

where $\boldsymbol{\mathcal{X}}^*$ is the input, $\mathbf{y}^*$ is its corresponding predicted output and $p(\mathbf{y}^*|\boldsymbol{\mathcal{X}}^*, \Omega)$ is the likelihood.

Unfortunately, direct inference of the posterior is intractable due to the large parameter space and nonlinear nature of DL architectures. A popular approximation technique, known as VI, formulates the problem of posterior inference as an optimization problem [49]. The VI approach considers a simple family of distributions over the network parameters and attempts to find a distribution, called the *variational*

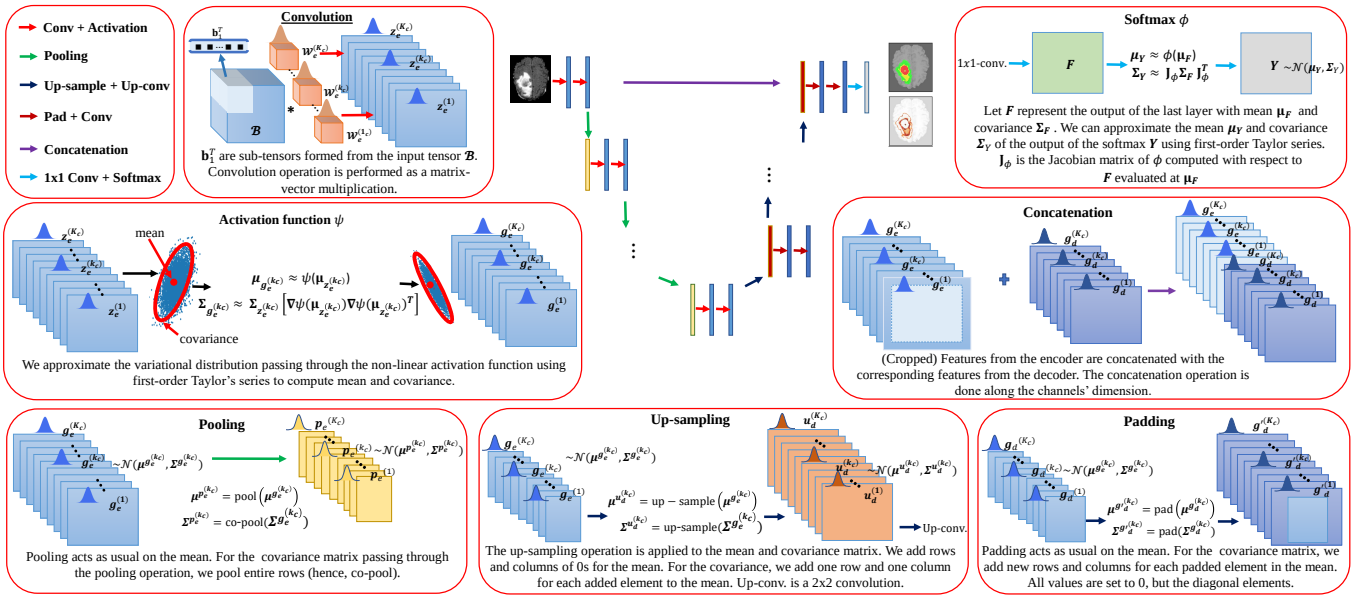


Fig. 1. An illustration of the SUPER-Net model. All mathematical operations are performed on random variables. The mean and covariance matrices are propagated through each operation. The output of SUPER-Net is the prediction (i.e., segmented image) and a covariance matrix (which, in turn, is used to create the uncertainty map associated with the prediction).

distribution $q_{\boldsymbol{\theta}}(\Omega)$, within this family that is "close" to the *true* unknown posterior. The notion of distributional closeness is captured by the Kullback-Leibler (KL) divergence and the optimization is performed with respect to the variational distribution parameters $\boldsymbol{\theta}$:

$$\mathbf{KL}\left(q_{\boldsymbol{\theta}}(\Omega)\middle|\middle|p(\Omega|\mathcal{D})\right) = \int q_{\boldsymbol{\theta}}(\Omega)\log\frac{q_{\boldsymbol{\theta}}(\Omega)}{p(\Omega)p(\mathcal{D}|\Omega)}d\Omega. \quad (2)$$

By rearranging terms in (2), the well-known ELBO objective function is obtained [13]:

$$\mathcal{L}(\boldsymbol{\theta}) = -\,\mathbb{E}_{q_{\boldsymbol{\theta}}(\Omega)}\left[\log(p(\mathcal{D}|\Omega)\right] + \mathbf{KL}\left(q_{\boldsymbol{\theta}}(\Omega)\middle|\middle|p(\Omega)\right). \quad (3)$$

Most Bayesian DL frameworks that use the VI approach sample one set of parameters $\boldsymbol{\theta}$ and perform a deterministic forward pass and backpropagation. The second moment or the variance of the predictive distribution is obtained post-training using MC samples at inference time [50]. This practice is based on the assumption that the single set of sampled parameters $\boldsymbol{\theta}$ represents the variational distribution $q_{\boldsymbol{\theta}}(\Omega)$ with sufficient accuracy, which has no theoretical grounds [14].

C. Encoder Operations

We define a multivariate Gaussian distribution as a prior distribution for all convolution kernels. We assume that kernels are independent within each layer as well as across layers in both the encoder and decoder paths. The independence assumption results in a single additional parameter (i.e., variance) for each kernel, limiting the increase in the number of parameters due to the Bayesian formulation. Moreover, independent kernels help extract uncorrelated features and better explore the input space [14].

1) Convolution Between Input and Network Parameters: The convolution operation in the first layer is performed between the input data (initially assumed deterministic for simplicity) and the network parameters (random variables). We assume that network parameters $\boldsymbol{\mathcal{W}}_e^{(k_1)}$ follow a Gaussian distribution, i.e., $\text{vec}(\boldsymbol{\mathcal{W}}_e^{(k_1)}) \sim \mathcal{N}\left(\mathbf{m}_e^{(k_1)}, \boldsymbol{\Sigma}_e^{(k_1)}\right)$. We write the convolution as a matrix-vector multiplication, where $\mathbf{X}$ denotes the matrix having rows equal to the vectorized sub-tensors of the input $\boldsymbol{\mathcal{X}}$. Then, the convolution operation is expressed as $\mathbf{z}_e^{(k_1)} = \mathbf{X} \times \text{vec}(\boldsymbol{\mathcal{W}}_e^{(k_1)})$, for $k_1 = 1, \cdots, K_1$. Thus, the output of the first convolutional layer follows a Gaussian distribution where the mean and covariance are given by:

$$\mathbf{z}_e^{(k_1)} \sim \mathcal{N}\left(\mathbf{X}\mathbf{m}_e^{(k_1)},\ \mathbf{X}\boldsymbol{\Sigma}_e^{(k_1)}\mathbf{X}^T\right). \quad (4)$$

2) Convolution Between Two Random Variables: We consider a generic case of convolution between two random variables. Let $\boldsymbol{\mathcal{B}}$ be the incoming input to any convolution layer, except the first layer, i.e., $c \neq 1$. The convolution operation is expressed as a matrix-vector multiplication; however, in this case both the input and the kernels are random tensors. We form $\mathbf{B}$ by vectorizing the sub-tensors of the incoming input $\boldsymbol{\mathcal{B}}$, i.e., $\mathbf{B} = [\mathbf{b}_1^T, \mathbf{b}_2^T, \cdots, \mathbf{b}_J^T]^T$, where $\mathbf{b}_j^T$ represents j^{th} row of $\mathbf{B}$. Let $\boldsymbol{\mu}_{\mathbf{b}_j}$ and $\boldsymbol{\Sigma}_{\mathbf{b}_j}$ represent the mean and covariance of $\mathbf{b}_j$. Then, the output of the convolution is formulated as $\mathbf{z}_e^{(k_c)} = \mathbf{B} \times \text{vec}(\boldsymbol{\mathcal{W}}_e^{(k_c)})$ with $\text{vec}(\boldsymbol{\mathcal{W}}_e^{(k_c)}) \sim \mathcal{N}\left(\mathbf{m}_e^{(k_c)}, \boldsymbol{\Sigma}_e^{(k_c)}\right)$ for $k_c = 1, \cdots, K_c$. Given that the input $\boldsymbol{\mathcal{B}}$ (feature map) is independent from the subsequent layer kernels, we compute elements of the mean of $\mathbf{z}_e^{(k_c)}$ as the product of the two mean vectors, $\boldsymbol{\mu}_{\mathbf{b}_j}$ and $\mathbf{m}_e^{(k_c)}$, i.e.,

$$[\boldsymbol{\mu}_{\mathbf{z}_e^{(k_c)}}]_j = \boldsymbol{\mu}_{\mathbf{b}_j}^T \mathbf{m}_e^{(k_c)}, \quad j = 1, \cdots, J. \quad (5)$$

The elements of the covariance matrix $\mathbf{\Sigma}_{\mathbf{z}_e^{(k_c)}}$ are derived as:

Non-diagonal elements $(i \neq j)$:

$$\boldsymbol{\mu}_{\mathbf{b}_i}^T \mathbf{\Sigma}_e^{(k_c)} \boldsymbol{\mu}_{\mathbf{b}_j}, \tag{6}$$

Diagonal elements $(i = j)$:

$$\mathrm{Tr}\left(\mathbf{\Sigma}_{\mathbf{b}_i} \mathbf{\Sigma}_e^{(k_c)}\right) + \boldsymbol{\mu}_{\mathbf{b}_i}^T \mathbf{\Sigma}_e^{(k_c)} \boldsymbol{\mu}_{\mathbf{b}_j} + \mathbf{m}_e^{(k_c)T} \mathbf{\Sigma}_{\mathbf{b}_j} \mathbf{m}_e^{(k_c)}. \tag{7}$$

3) Nonlinear Activation Function: Convolutional layers are commonly followed by an element-wise nonlinear activation function, e.g., Rectified Linear Unit (ReLU). Let ψ denote the activation function and $\mathbf{g}_e^{(k_c)}$ denote the output of the activation function, i.e., $\mathbf{g}_e^{(k_c)} = \psi[\mathbf{z}_e^{(k_c)}]$ for $k_c = 1, \cdots, K_c$. We use the first-order Taylor series approximation to derive the mean and covariance of the random variable $\mathbf{g}_e^{(k_c)}$, i.e.,

$$\boldsymbol{\mu}_{\mathbf{g}_e^{(k_c)}} \approx \psi\big(\boldsymbol{\mu}_{\mathbf{z}_e^{(k_c)}}\big), \tag{8}$$

$$\mathbf{\Sigma}_{\mathbf{g}_e^{(k_c)}} \approx \mathbf{\Sigma}_{\mathbf{z}_e^{(k_c)}} \odot \left[\nabla\psi\big(\boldsymbol{\mu}_{\mathbf{z}_e^{(k_c)}}\big) \nabla\psi\big(\boldsymbol{\mu}_{\mathbf{z}_e^{(k_c)}}\big)^T\right], \tag{9}$$

where ∇ is the gradient with respect to $\mathbf{z}_e^{(k_c)}$.

4) Max-Pooling Operation: The max-pooling operation is often used to downsample the incoming feature map. We propagate the mean through the max-pooling layer using the classical operation of selecting the largest value from a patch in the feature map. The pooling for the covariance is achieved by only retaining the rows and columns (of the incoming covariance matrix) corresponding to the retained elements (pooled elements) of the mean vector. We write the mean and covariance as follows:

$$\boldsymbol{\mu}_{\mathbf{p}_e^{(k_c)}} = \text{pool}(\boldsymbol{\mu}_{\mathbf{g}_e^{(k_c)}}), \tag{10}$$

$$\mathbf{\Sigma}_{\mathbf{p}_e^{(k_c)}} = \text{co-pool}(\mathbf{\Sigma}_{\mathbf{g}_e^{(k_c)}}). \tag{11}$$

An encoder may consist of multiple layers of convolution operations, nonlinear activation functions, and max-pooling to get a low-dimensional representation of the input.

D. Decoder Operations

The operations in the decoder path start with the low-dimensional representation produced by the encoder. The decoder may also include multiple convolutional layers, which are performed following the mathematical relationships provided in Eqs. (5)-(7).

1) Up-sampling: The up-sampling is an essential part of the decoder path that increases the resolution of the input. Using $\mathbf{g}_d^{(k_c)}$ to represent the input to the up-sampling operation and $\mathbf{u}_d^{(k_c)}$ as the output, we have:

$$\mathbf{u}_d^{(k_c)} = \text{up-sample}\left(\mathbf{g}_d^{(k_c)}\right). \tag{12}$$

The mean of $\mathbf{u}_d^{(k_c)}$ is computed by inserting zeros between two consecutive elements of the input and padding with zeros. The covariance matrix is obtained by adding rows and columns of zeros at locations corresponding to the newly added zeros in the mean.

2) Up-convolution: The up-sampling operation may produce sparse feature maps with many zeros. Generally, a 2×2 convolution operation is performed to get a dense high-resolution output. The mean and covariance are computed using results presented in Eqs. (5)-(7).

3) Padding: The padding operation applied to the mean is the same as the classical zero-padding operation. For the covariance matrix, we add a new row and a new column for each element padded to the mean. The new elements added in the covariance matrix are all set to zero and the variance (diagonal) elements are set to a user-defined small value with $\sigma_{pa} > 0$.

4) Concatenation: The features from the encoder side are generally concatenated with the corresponding features from the decoder to improve localization of various objects in the input. The feature maps from the encoder path may need to be resized or cropped before they can be concatenated with the decoder features due to the differences in size.

Let $\mathcal{G}_e^c$ be the c^{th} encoder feature map, and $\mathbf{g}_e^{(k_c)}$ the k_c^{th} slice from such map with mean and covariance $\boldsymbol{\mu}_{\mathbf{g}_e^{(k_c)}}$ and $\mathbf{\Sigma}_{\mathbf{g}_e^{(k_c)}}$, respectively. The cropped feature map is denoted with $\mathcal{G}_e^{*c}$ where k_c^{th} slice is $\mathbf{g}_e^{*(k_c)}$. For $k_c = 1, \ldots, K_c$, $\boldsymbol{\mu}_{\mathbf{g}_e^{*(k_c)}} = \text{crop}(\boldsymbol{\mu}_{\mathbf{g}_e^{(k_c)}})$ while $\mathbf{\Sigma}_{\mathbf{g}_e^{*(k_c)}}$ is obtained by removing the rows and columns from $\mathbf{\Sigma}_{\mathbf{g}_e^{(k_c)}}$ corresponding to the cropped elements of $\boldsymbol{\mu}_{\mathbf{g}_e^{(k_c)}}$.

The output of the concatenation operation is a feature map $\mathcal{G}_d^{*c} = \{\mathcal{G}_d^c, \mathcal{G}_e^{*c}\}$, where $\mathcal{G}_d^c$ is the c^{th} decoder feature map. The concatenation operation is done along the dimension that represents channels in the feature maps (generally the third dimension).

5) Softmax Function: Pixel-level segmentation can be considered as a dense classification problem where we assign a label to each pixel. Hence, for a multi-class problem, a softmax function ϕ is applied to the output of the last layer.

Let $\mathbf{F}$ represent the output of the last layer with mean $\boldsymbol{\mu}_{\mathbf{F}}$ and covariance $\mathbf{\Sigma}_{\mathbf{F}}$, and $\mathbf{Y}$ denote the output of the network after the softmax operation. We can approximate the mean $\boldsymbol{\mu}_{\mathbf{Y}}$ and covariance $\mathbf{\Sigma}_{\mathbf{Y}}$ using first-order Taylor series, that is:

$$\boldsymbol{\mu}_{\mathbf{Y}} \approx \phi(\boldsymbol{\mu}_{\mathbf{F}}), \tag{13}$$

$$\mathbf{\Sigma}_{\mathbf{Y}} \approx \boldsymbol{J}_\phi \mathbf{\Sigma}_{\mathbf{F}} \boldsymbol{J}_\phi^T, \tag{14}$$

where $\boldsymbol{J}_\phi$ is the Jacobian matrix of ϕ computed with respect to $\mathbf{F}$ evaluated at $\boldsymbol{\mu}_{\mathbf{F}}$.

The mathematical results presented above for various operations can be used to build any type of deep neural network in addition to the proposed encoder-decoder based segmentation networks.

IV. Experimental Methods

We focus on medical image segmentation for validating the efficacy of the proposed SUPER-Net framework. We apply the proposed SUPER-Net framework to the U-Net architecture; for simplicity, we refer to it as SUPER U-Net. We employ three different datasets and compare SUPER U-Net with three state-of-the-art segmentation networks, a deterministic U-Net, a Bayes U-Net obtained using MC dropout, and an Ensemble U-Net [28], [33], [45].

A. Segmentation Network Architectures

1) U-Net - The Base Segmentation Architecture: Among all architectures proposed for medical image segmentation,

U-Net is the most widely used [28]. U-Net is built using the encoder-decoder structure with a contracting path that is almost identical to the expanding path. The contracting path may consist of multiple encoder blocks, which, in turn, may include various convolution layers, max-pooling, and nonlinear activations. The expanding path consists of multiple decoder blocks, which are made of multiple layers of convolution, activation functions, up-convolution, up-sampling and padding. Additionally, there are connections between the encoder and decoder blocks that concatenate feature maps from the encoder with the corresponding feature maps of the decoder. Finally, a 1×1 convolution and softmax are applied to the decoded feature maps before calculating the cross-entropy loss function.

In the original U-Net architecture [28], the border pixels are lost due to un-padded convolution operations and the missing regions are extrapolated by mirroring. Such processing may yield erroneous results for some medical image segmentation datasets. Hence, in our setting, we apply the padding operation to increase the size of the feature maps and reconstruct the full image at the output of the network. We include the padding operation twice in each decoder block on the expanding path. The first padding operation is performed before the concatenation and the second is performed before the second convolution in each decoder block. In our experiments, we refer to this U-Net architecture as the deterministic segmentation network.

2) Bayes U-Net: Bayes U-Net is built using the MC dropout technique following the implementation of [33]. The dropout is used only in the central blocks with the probability of dropping a neuron set to $p = 0.5$. Bayes U-Net uses cross-entropy loss function. At the inference time, we use $N = 20$ MC samples and the uncertainty is measured in terms of predictive entropy (PE) [10].

3) Ensemble U-Net: Ensemble U-Net is built using an ensemble of U-Net models. We trained 5 networks with different initializations and using the entire training set for each model. The number of networks is chosen following the results in [40], [45]. Ensemble U-Net uses the cross-entropy loss function. At inference time, each input is fed to the five models and the outputs are used to estimate uncertainty using the PE.

4) SUPER U-Net: SUPER U-Net uses the mathematical operations presented in Sections III-C and III-D to propagate the first two moments of the variational distribution through the U-Net architecture. The output of SUPER U-Net consists of a segmentation map and an uncertainty map. The former is given by the mean of the predictive distribution, while the latter is generated by the covariance of the predictive distribution. We use a Gaussian variational distribution and employ the ELBO loss function defined in Eq. (3). We optimize the ELBO loss function with respect to the variational parameters, i.e., the mean and covariance of the variational distribution. To reduce the computational complexity, we propagate diagonal covariance matrices.

B. Datasets and Models

We use three different medical segmentation datasets, including lung CT, hippocampus MRIs and brain tumor MRIs [51]–[53]. Our experiments use only the publicly available annotated data from the respective datasets, i.e., unlabeled data is not used for training or validation. The datasets are divided into training, validation and testing bins with approximately 80% selected for training, 10% for validation and 10% for testing.

1) Lungs Dataset: The dataset includes 20 CT scans from the chest region, including the lungs. This heterogeneous dataset consists of both COVID-19 and non-COVID-19 patients. The data annotations include left lung, right lung and infections (if found). We consider a binary segmentation task for this dataset, i.e., delineating the boundaries of the lungs in the given CT images. We assign a label of 0 to the background and 1 to lung tissue. The pre-processing steps include: 1) windowing the Hounsfield units range between -1250 and 250; 2) normalizing all pixel values between 0 and 1; 3) deleting empty slices, i.e., slices that include only the label 0 corresponding to the background; and 4) cropping all images to a single size, i.e., 512×512 pixels.

The U-Net architecture used for this dataset includes 3 encoder blocks and 2 decoder blocks. The number of kernels in the encoder blocks is set to 16, 32, and 64, while to 32 and 16 in the decoder blocks. We train all four networks (i.e., U-Net, Bayes U-Net, Ensemble U-Net and SUPER U-Net) for 50 epochs using a batch size of 10 with the Adam optimizer and a learning rate of 0.001 with a learning rate scheduler. In VMP U-Net, we set $\sigma_{pa} = 0.1$.

2) Hippocampus Dataset: The dataset consists of 394 single-modality MRI scans. The segmentation task requires the precise delineation of two adjacent structures, i.e., anterior (label 1) and posterior (label 2). The pre-processing steps include: 1) normalizing the data to reduce the image bias (which is a characteristic of MRI data); 2) deleting empty slices, i.e., those that include only the background; and 3) padding images to have the same input size of 64×64 pixels.

For the hippocampus task, the U-Net architecture consists of 3 encoder blocks and 2 decoder blocks. The convolutional kernels are set to 32, 64, and 128 on the encoder side and 64, and 32 on the decoder side. All four networks (i.e., U-Net, Bayes U-Net, Ensemble U-Net and SUPER U-Net) are trained with Adam optimizer for a total of 100 epochs using a batch size of 20. In SUPER U-Net, we set $\sigma_{pa} = 0.02$.

3) Brain Tumor Segmentation (BraTS) Dataset: The dataset includes about 300 multi-modal (T1, T1c, T2, and FLAIR) MRI scans from 274 brain tumor patients (some patients have multiple MRI scans) [53]. The dataset is divided into two main types of tumors, low-grade gliomas (LGG) and high-grade gliomas (HGG). We focus on the more challenging HGG dataset in our experiments. The pre-processing steps include: 1) normalizing data to reduce the image bias; 2) deleting images that do not include any tumor structure; and 3) cropping each image to the size of 240×240 pixels. The input data size for each sample in the dataset is $240 \times 240 \times 4$ pixels, where the last number represents the four modalities, i.e., T1, T1c, T2, and FLAIR. All four networks (U-Net, Bayes U-Net, and SUPER U-Net) are trained to segment 5 different labels in the HGG MRIs, i.e., normal tissue (label 0), necrosis (label 1), edema (label 2), non-enhancing tumor (label 3),

TABLE I
DSC FOR LUNGS DATASET - PERFORMANCE COMPARISON OF DIFFERENT NETWORKS UNDER ADDITIVE GAUSSIAN NOISE.

	U-Net	Bayes U-Net	Ensemble U-Net	SUPER U-Net
Noise Free	**.83**	**.83**	**.83**	**.83**
Gaussian noise added to the entire image				
SNR $\approx$ 35 dB	.82	.82	.82	**.83**
SNR $\approx$ 3 dB	.16	.19	.11	**.21**
Gaussian noise added to lung pixels only				
SNR $\approx$ 31 dB	.82	**.83**	**.83**	**.83**
SNR $\approx$ 14 dB	.63	.63	.65	**.79**

and enhancing tumor (label 4). In most clinical applications, generally, three tumor regions are considered for evaluating the results of segmentation, whole tumor (labels 1, 2, 3 and 4), tumor core (labels 1, 3 and 4), and enhancing tumor region (label 4) [53].

We use the original U-Net architecture with 5 encoder and 4 decoder blocks [28]. The number of kernels in each encoder block is 64, 128, 256, 512, and 1024. The number of kernels used in the decoder blocks is 512, 256, 128, and 64. We set $\sigma_{pa} = 0.1$ for the SUPER U-Net. All four networks are trained for 100 epochs using Adam optimizer with a learning rate of 0.001 and a batch size of 20.

4) Clinical Dataset: - The imaging dataset includes 627 fluid attenuated inversion recovery (FLAIR) sequences, including 24 images each on average, from patients diagnosed with World Health Organization grade 2 gliomas, seen at the neuro-oncology clinics at the University of Alabama at Birmingham (see [54]). The tumor masks were generated by an expert physician.

We use a modified U-Net architecture with 5 encoder blocks made of one convolution with padding set to "*same*", batch-normalization, ReLU activation and a max-pooling operation. The 4 decoder blocks are built with an up-sampling followed by a 2×2 convolution, a convolution with padding set to "*same*", batch-normalization and ReLU activation function. The number of kernels in each encoder block is 16, 32, 64, 128, and 256. The number of kernels used in the decoder blocks is 128, 64, 32, and 16.

C. Other Experimental Settings

We report the Dice Similarity Coefficient (DSC) as the metric to compare the performance of all four networks. Additionally, we perform an evaluation of all approaches in terms of over-segmentation and under-segmentation performance, and we report it in appendix B.

Although the choice of the loss function can impact the performance of the network, there is no consensus on the best performing loss function as it depends on the dataset and the specific task [45], [55]–[57]. For example, the loss function based on DSC may result in slightly (or marginal) better performance as compared to the cross-entropy loss [56], but it can produce miscalibrated models with MC dropout [57]. In our experiments, we used the same loss function, i.e., cross-entropy, for U-Net, Bayes U-Net and Ensemble U-Net.

We conduct a detailed robustness analysis of the performance of all four networks using several types of noise. We report two types of noise, i.e., Gaussian and adversarial, while additional results are presented in the appendix A. We compare the performance of all four networks under various levels of Gaussian noise added to the test data of all three datasets. We measure the noise level using the Signal-to-Noise Ratio (SNR) in the units of decibels (dB). For the adversarial noise, we use the Fast Gradient Sign Method (FSGM) to generate untargeted attacks [58], and we use the Projected Gradient Descent (PGD) method to generate targeted adversarial attacks [59]. The attacks are generated with a maximum number of iterations set to 20 and a step-size of 1. We select a *source* class and a *target* class to generate targeted attacks. The adversarial attack algorithm will try to fool the trained network into predicting pixels belonging to the *source* class as the pixels of the *target* class.

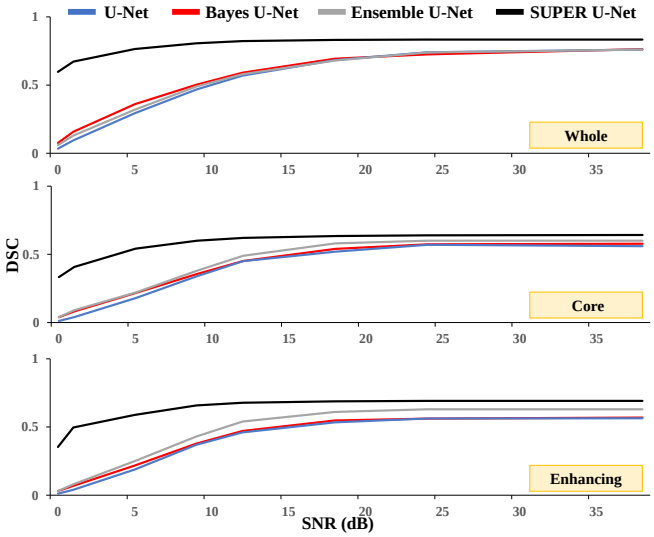


Fig. 2. Performance of the four networks, i.e., U-Net (blue), Bayes U-Net (red), Ensemble U-Net (gray) and SUPER U-Net (black), under various levels of Gaussian noise added to the BraTS test data. The three sub-plots show the Dice Similarity Coefficient (DSC) values for a range of Signal to Noise Ratios (SNRs) for three different tumor regions: whole tumor, core, and enhancing.

V. RESULTS AND DISCUSSION

We report our results in three parts. First, we present the performance analysis (measured using DSC) of the four networks (U-Net, Bayes U-Net, Ensemble U-Net, and SUPER U-Net) under various levels of Gaussian noise added to the test data. Next, we analyze the same four networks under various levels of targeted and untargeted adversarial attacks. Finally, we present an analysis of the uncertainty maps and the predictive variance generated by the proposed SUPER U-Net at inference time.

A. Evaluation Under Gaussian Noise

Tables I, II, and III report DSC values for U-Net, Bayes U-Net, Ensemble U-Net and SUPER U-Net under different levels of Gaussian noise, including the noise-free case. For each dataset, we report results for two cases, i.e., noise added to the entire input image or only to the structures that the networks are trying to segment, e.g., tumor in the BraTS dataset.

TABLE II
DSC FOR HIPPOCAMPUS DATASET - PERFORMANCE COMPARISON UNDER ADDITIVE GAUSSIAN NOISE.

	Anterior				**Posterior**			
	U-Net	**Bayes U-Net**	**Ensemble U-Net**	**SUPER U-Net**	**U-Net**	**Bayes U-Net**	**Ensemble U-Net**	**SUPER U-Net**
Noise Free	**.79**	**.79**	**.79**	**.79**	.76	.76	**.77**	.74
Gaussian noise added to entire image								
SNR $\approx$ 23 dB	.77	.77	.77	**.78**	.74	**.75**	.73	.73
SNR $\approx$ 15 dB	.49	.53	.53	**.69**	.54	.43	.53	**.64**
SNR $\approx$ 8 dB	.09	.12	.10	**.36**	.13	.07	.12	**.28**
Gaussian noise added to Anterior pixels only								
SNR $\approx$ 30 dB	.69	.73	.72	**.75**	**.76**	.75	**.76**	.74
SNR $\approx$ 24 dB	.35	.47	.41	**.57**	**.74**	.73	**.74**	**.74**
SNR $\approx$ 18 dB	.05	.11	.07	**.22**	.67	.69	.69	**.70**
Gaussian noise added to Posterior pixels only								
SNR $\approx$ 30 dB	**.79**	.78	**.79**	**.79**	.67	.66	**.68**	.67
SNR $\approx$ 24 dB	**.78**	**.78**	**.78**	**.78**	.22	.40	.38	**.46**
SNR $\approx$ 18 dB	.74	.75	.75	**.76**	.02	.07	.06	**.20**

TABLE III
DSC FOR BRATS DATASET - PERFORMANCE COMPARISON UNDER ADDITIVE GAUSSIAN NOISE.

	Whole				***Core***				***Enhancing***			
	U-Net	**Bayes U-Net**	**Ensemble U-Net**	**SUPER U-net**	**U-Net**	**Bayes U-Net**	**Ensemble U-Net**	**SUPER U-net**	**U-Net**	**Bayes U-Net**	**Ensemble U-Net**	**SUPER U-net**
Noise free	.77	.77	.76	**.83**	.58	.58	.60	**.64**	.57	.57	.63	**.69**
Gaussian noise added to entire image												
SNR $\approx$ 24 dB	.73	.74	.74	**.83**	.57	.57	.60	**.64**	.56	.56	.63	**.69**
SNR $\approx$ 18 dB	.68	.69	.68	**.83**	.54	.55	.57	**.63**	.54	.55	.61	**.69**
SNR $\approx$ 9 dB	.49	.50	.48	**.81**	.35	.36	.38	**.60**	.38	.38	.43	**.66**
Gaussian noise added to tumor pixels only												
SNR $\approx$ 32 dB	.70	.70	.69	**.83**	.54	.55	.58	**.64**	.55	.55	.61	**.68**
SNR $\approx$ 25 dB	.62	.62	.60	**.83**	.48	.48	.50	**.64**	.49	.49	.55	**.64**
SNR $\approx$ 13 dB	.21	.22	.21	**.79**	.11	.11	.15	**.46**	.10	.10	.12	**.37**

TABLE IV
DSC FOR LUNGS DATASET - PERFORMANCE COMPARISON UNDER UNTARGETED ADVERSARIAL ATTACKS.

	U-Net	**Bayes U-Net**	**Ensemble U-Net**	**SUPER U-Net**
Noise Free	**.83**	**.83**	**.83**	**.83**
Untargeted attacks generated using FGSM				
SNR $\approx$ 55 dB	.80	**.82**	**.82**	**.82**
SNR $\approx$ 29 dB	.55	.64	.58	**.67**
SNR $\approx$ 10 dB	.21	.35	.22	**.44**

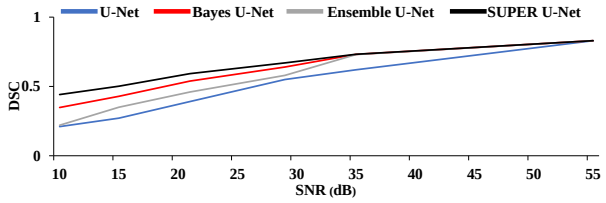


Fig. 3. Performance of four networks, i.e., U-Net (blue), Bayes U-Net (red), Ensemble U-Net (gray) and SUPER U-Net (black), under various levels of untargeted attacks to the Lungs test data. We plot the DSC vs SNR (dB) for the 4 approaches. The y-axis displays the Dice Similarity Coefficient (DSC) at test time versus vs Signal to Noise Ratio (SNR), measured in dB.

We note that the proposed SUPER U-Net generally demonstrates more robust behavior as compared to deterministic U-Net, Bayes U-Net, and Ensemble U-Net especially at low SNR values, i.e., high levels of noise. In Fig. 2, we plot DSCs vs. SNR for the three tumor regions. Each subplot compares the performance of the four networks for multiple levels of Gaussian noise added to the entire image.

B. Evaluation Under Adversarial Attacks

We assess the robustness of all four networks against targeted and untargeted adversarial attacks in Tables IV, V, and VI. The tables present DSC values for various levels of adversarial attacks, quantified using SNR. We observe that SUPER U-Net shows better performance (i.e., high DSC values) as compared to the other three networks, especially for stronger attacks (i.e., low values of SNR).

In Fig. 3, we show DSC values for a range of untargeted adversarial attacks, generated using FGSM, against the lung test dataset. We plot the DSC vs. SNR for the four approaches.

C. Evaluation of the Clinical Data

We show that SUPER U-Net can scale to real world datasets. SUPER U-Net is able to achieve 86% DSC on held-on test data. Figure 6 shows sample scans from the UAB clinical data (first column) along with ground-truth segmentations (second column) and SUPER U-Net's segmentations and associated uncertainty maps (third and fourth columns, respectively). The representative images show that SUPER U-Net is uncertain when a tumor region is missed (scans 1 and 2), as well as for unusually low signal pixels within

TABLE V
DSC FOR HIPPOCAMPUS DATASET - PERFORMANCE COMPARISON UNDER VARIOUS LEVELS OF TARGETED ADVERSARIAL ATTACKS.

	Anterior				***Posterior***			
	U-Net	**Bayes U-Net**	**Enseble U-Net**	**SUPER U-Net**	**U-Net**	**Bayes U-Net**	**Ensemble U-Net**	**SUPER U-Net**
Noise Free	**.79**	**.79**	**.79**	**.79**	.76	.76	**.77**	.74
Targeted adversarial attacks - source: label 1, target: label 2								
SNR $\approx$ 29 dB	.75	**.76**	.75	.75	.60	.60	**.64**	**0.64**
SNR $\approx$ 23 dB	.71	**.72**	**.72**	**.72**	.52	.55	.58	**.59**
SNR $\approx$ 15 dB	.40	.45	.48	**.52**	.19	.27	.32	**.34**
Targeted adversarial attacks - source: label 2, target: label 1								
SNR $\approx$ 29 dB	.65	**.69**	**.69**	**.69**	.67	**.71**	**.71**	**.71**
SNR $\approx$ 23 dB	.59	.64	.55	**.65**	.65	**.70**	.65	**.70**
SNR $\approx$ 15 dB	.21	.32	.34	**.42**	.39	.40	.44	**.46**

TABLE VI
DSC FOR BRATS DATASET - PERFORMANCE COMPARISON UNDER VARIOUS LEVELS OF UNTARGETED AND TARGETED ADVERSARIAL ATTACKS.

	Whole				***Core***				***Enhancing***			
	U-Net	**Bayes U-Net**	**Ensemble U-Net**	**SUPER U-net**	**U-Net**	**Bayes U-Net**	**Ensemble U-Net**	**SUPER U-net**	**U-Net**	**Bayes U-Net**	**Ensemble U-Net**	**SUPER U-net**
Noise free	.77	.77	.76	**.83**	.58	.58	.60	**.64**	.57	.57	.63	**.69**
Untargeted attacks generated using FGSM												
SNR $\approx$ 39 dB	.67	.68	.70	**.82**	.46	.47	.56	**.62**	.46	.46	.58	**.64**
SNR $\approx$ 12 dB	.34	.37	.35	**.58**	.20	.23	.24	**.31**	.19	.20	.25	**.30**
Targeted adversarial attacks - source: label 3, target: label 1												
SNR $\approx$ 44 dB	.69	.70	.73	**.82**	.48	.50	.58	**.61**	.48	.50	.62	**.67**
SNR $\approx$ 19 dB	.34	.35	.52	**.55**	.22	.23	.34	**.35**	.24	.24	.34	**.36**
Targeted adversarial attacks - source: label 1, target: label 3												
SNR $\approx$ 44 dB	.70	.71	.73	**.82**	.50	.50	.59	**.63**	.48	.49	.61	**.67**
SNR $\approx$ 19 dB	.38	.38	.52	**.56**	.24	.25	.34	**.35**	.25	.26	.35	**.37**
Targeted adversarial attacks - source: label 3, target: label 2												
SNR $\approx$ 44 dB	.70	.71	.73	**.82**	.52	.53	.59	**.64**	.50	.53	.62	**.67**
SNR $\approx$ 19 dB	.35	.35	.52	**.54**	.24	.24	.35	**.36**	.24	.25	.38	**.39**
Targeted adversarial attacks - source: label 2, target: label 3												
SNR $\approx$ 44 dB	.70	.71	.73	**.82**	.51	.53	.59	**.62**	.51	.52	.62	**.68**
SNR $\approx$ 19 dB	.35	.35	.52	**.58**	.23	.24	.35	**.37**	.25	.26	.34	**.38**

the tumor (scan 1). A typical tumor is associated with high FLAIR signal; in the first scan, the central part of the tumor is associated with a low signal, which is atypical (see right arrow in Fig. 6, row 1, column 4). In a sense, the model is attracting the physician's attention to these regions in the image so that they can confirm whether these are part of the tumor or not. In the second scan, the tumor is totally missed, but the model exhibits high uncertainty in the missed region. The last scan has no tumor and SUPER-Net predicts correctly true negative cases and associates a very low uncertainty (predictive variance 0) or equivalently a high confidence in these predictions.

D. Uncertainty Maps and Predictive Variance – Quantitative Analysis

1) Uncertainty Maps: The output of SUPER U-Net consists of the pair: segmentation map (prediction) and uncertainty map (obtained from the predictive covariance). For the other approaches, uncertainty is evaluated through multiple forward passes. In Fig. 4, and 5, we present representative cases selected from the hippocampus and BraTS test data. We show the input modality (only FLAIR for the BraTS data), the ground-truth label, and predictions with associated uncertainty maps. The first row presents the noise-free case, the second row reports the predictions and uncertainty maps for the Gaussian noise case, and the third and fourth rows show two examples of adversarial attacks. We normalized the predictive variance of SUPER U-Net for better visual comparison to the uncertainty maps of Bayes U-Net and Ensemble U-Net. We point to regions (pixels) incorrectly classified by our network with the black arrows, and we point to the corresponding locations in the uncertainty maps. It is evident from the figure that SUPER U-Net associates high uncertainty with incorrect predictions and pixels belonging to targeted regions.

2) Predictive Variance – Quantitative Analysis: We investigate the response of the derived second moment (variance/uncertainty) and relate it to the model's performance (DSC). We calculate the average predictive variance from uncertainty maps and plot these values against various levels of Gaussian noise in Fig. 7, and adversarial attacks in Fig. 8, for hippocampus and BraTS datasets. It is more instructive and insightful if sub-plots in both figures are interpreted from right to left, i.e., decreasing SNR or equivalently increasing noise in the test data. We note that the predictive variance increases monotonically with increasing noise (i.e., decreasing SNR) for all three sub-figures in Fig. 7 and all four sub-figures in Fig. 8. This behavior, i.e., increasing uncertainty with increasing noise, demonstrates that the network is aware of higher noise in the input. A useful and meaningful uncertainty estimate should convey a lower confidence/ higher uncertainty for low-

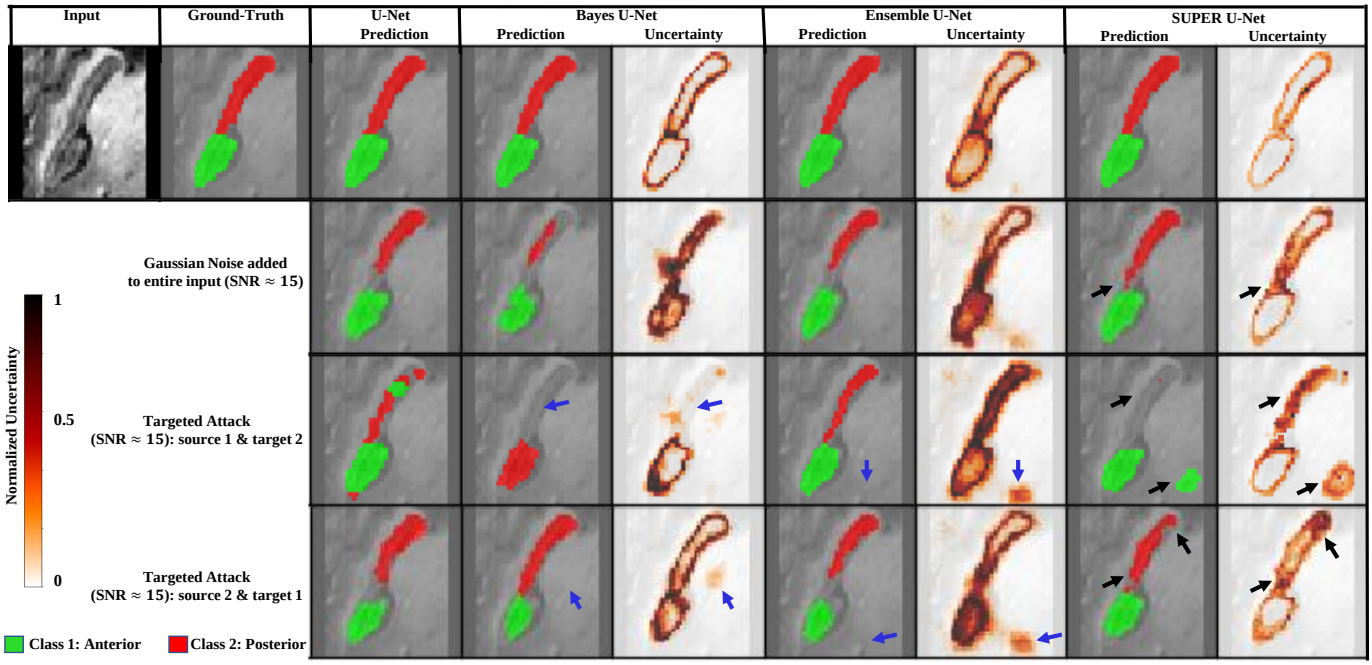


Fig. 4. Segmentation of the hippocampus test data. The first row shows (left to right) the input image, the ground-truth segmentation, noise-free segmentation predictions of the four models, i.e., U-Net, Bayes U-Net, Ensemble U-Net, and SUPER U-Net). The uncertainty map of each Bayesian model is shown next to the corresponding prediction. Rows $2, 3, 4$ display the segmented predictions along with their uncertainty maps (when applicable) for additive Gaussian noise, and two adversarial attacks, respectively. The black arrows point to regions incorrectly classified by the network. Observe that the corresponding pixels in the uncertainty maps reflect low confidence or higher variance values. The blue arrows refer to inconsistent uncertainty estimates: low confidence associated to incorrect predictions or high uncertainty for correctly classified regions.

accuracy segmented images [60], [61]. For our SUPER U-Net, we report the average predictive variance for correctly classified and misclassified pixels on noise free Brats test set in Table VIII. Observe that the incorrect pixels are associated to high variance or less confident predictions.

Following the quantitative uncertainty evaluation task in the BRATS challenge [61], we compute the percentage change in DSCs when *uncertain* pixels are removed, and DSC is computed only using the remaining pixels. To define *uncertain* pixels, for each model, we set as threshold the average predictive uncertainty for correctly classified pixels for the noise free case. All pixels with an uncertainty value above this threshold are marked as uncertain and removed from the computation of the DSC. We report the change in DSCs in table VII. The sample scan corresponds to that provided qualitatively in Fig. 5. As we can see, our approach consistently produces higher (↑) DSCs after removing uncertain pixels, i.e., unlike other approaches, our predictive variance (uncertainty) is above the threshold only for incorrectly classified pixels. Such information is valuable for detecting when the network may fail, and its predictions may become untrustworthy.

E. Discussion

Our extensive analysis shows that SUPER U-Net has superior robustness to noise and adversarial attacks compared to state-of-the-art uncertainty quantification approaches. In the noise-free case, SUPER U-Net performance is equivalent to the state-of-the-art models. However, as the noise level increases (Gaussian or adversarial), the task or the dataset becomes more complicated, e.g., BraTS data (multiple segmentation labels and multiple modalities), SUPER U-Net outperforms both the deterministic U-Net and other Bayesian approaches, i.e., Bayes U-Net and Ensemble U-Net. The superior performance and robustness to noise, especially at high levels of noise and complex task/data, can be attributed to the intrinsic learning of the uncertainty during training through propagation of the covariance information (in addition to the mean). This is in contrast to post-hoc estimation of uncertainty using MC runs through the network or models averaging at the inference time.

1) The Significance of Uncertainty Information: The reliability of the segmentation predictions can be assessed using the uncertainty maps. This is evident from the comparison with the point-estimate approach, i.e., U-Net (figures 4, 5). SUPER U-Net associates higher uncertainty with the incorrect predictions and pixels or regions targeted by adversarial attacks (marked with black arrows). We also note that when the predicted segmentation is (almost) identical to the ground-truth, the model is confident in its segmentation predictions and exhibit uncertainty only at the boundary between the structure of interest ant the background. When the network's segmentation predictions are incorrect, or the input is pertubed by noise or adversarially attacked, SUPER U-Net associates higher uncertainty values with the predictions (rows 2 to 4). On the other hand, inspecting the maps generated using other probabilistic approaches, we see that their uncertainty maps do not convey the same level of insight on the trustworthiness of the predictions. Ideally, the model's uncertainty should

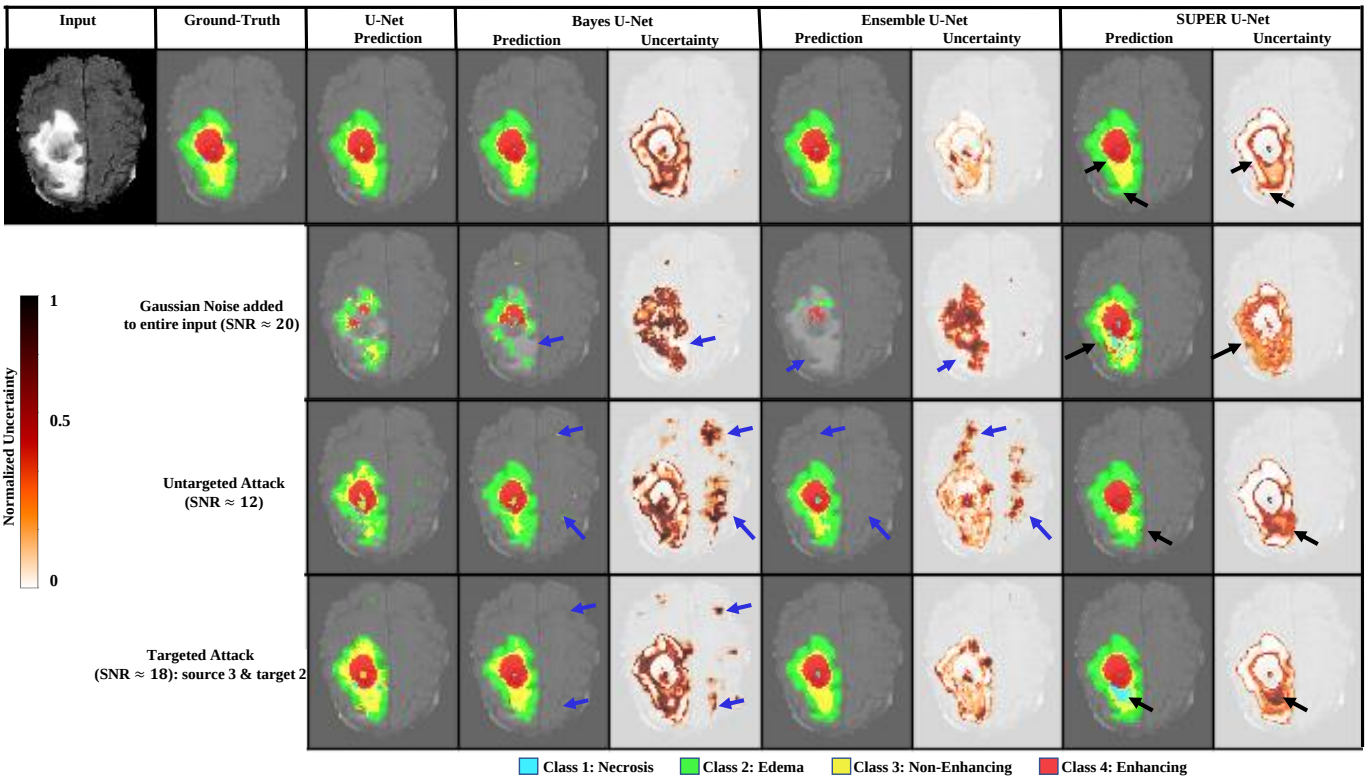


Fig. 5. Segmentation of the BraTS test data. The first row shows (left to right) the Flair input image, the ground-truth segmentation, noise-free segmentation predictions of the four models, i.e., U-Net, Bayes U-Net, Ensemble U-Net, and SUPER U-Net). The uncertainty map of each Bayesian model is shown next to the corresponding prediction. Rows $2, 3, 4$ display the segmented predictions along with their uncertainty maps (when applicable) for additive Gaussian noise, and two adversarial attacks, respectively. The black arrows point to regions incorrectly classified by the network. We note that the corresponding pixels in the uncertainty maps reflect the low confidence by responding with higher variance values. The blue arrows refer to inconsistent uncertainty estimates: low confidence associated to incorrect predictions or high uncertainty for correctly classified regions.

increase (darker red shades) only for regions of incorrect classification and/or for regions with noise or artifacts. However, as shown with the blue arrows in Figs. 4 and 5, both Bayes U-Net and Ensemble U-Net generate inconsistent uncertainty estimates: they associate low uncertainty (high confidence) to incorrect predictions and/or high uncertainty (low confidence) to correctly classified regions.

2) Clinical Impact: Coordinates of the tumor volume are used to determine the clinical target volume of the radiation therapy treatment. Inaccuracy and variation in defining critical volumes will affect everything downstream: treatment planning, dose-volume histogram analysis, and contour-based visual guidance used in image-guided radiation therapy. Studies have shown that undercoverage of radiation dose to the tumor target could compromise treatment outcomes [62]. Variations in manual contouring can be large [63]–[65]. Even with years of experience and skill, intra- and inter-observer variation of target volumes and organs remains substantial [66]–[69]. In [68], it was shown that the structure overlaps were as low as 10% and the volume variations had standard deviations up to 60%. A 2019 study showed that, although nearly all participants used identical guidelines for tumor delineation, there were large discrepancies in the volumes delineated [70]. The study concluded that "availability and implementation of guidelines alone is not enough to guarantee uniform delineation" [70]. A study of the variability in the target volumes for glioblastoma, determined and contoured by different radiotherapy facilities in Korea reported an average variability (using the Dice coefficient) of 23% [71]. Ultimately, both researchers and practitioners agree that radiotherapy is only as good as the accuracy with which the target is.

DL algorithms for segmentation have the potential to address the number one impediment to reliable use of imaging for guiding treatment planning of cancer, i.e., accurate and objective delineation of tumor from healthy tissue and organs. However, reliability and lack of consistency of DL predictions hinder the safe deployment of such models in the clinic. For example, a medical diagnostic system for detecting brain tumors from magnetic resonance scans may encounter a new tumor shape/structure (due to a different scan procedure) or an adversarial attack designed to fake a tumor for benefiting from medical bills [9]. Uncertainty information can limit the harmful consequences in such scenarios. Model confidence or uncertainty is critical when integrating the models in systems that make decisions that affect human life, either directly or indirectly. Ideally, the model should recognize the perturbed data and return an output (segmented image plus uncertainty map) that also conveys a high level of uncertainty.

SUPER U-Net simultaneously delivers the segmented image (prediction) along with the corresponding uncertainty map, which reflects the network's own confidence in the prediction of every pixel. For example, in figure 6, the SUPER U-Net

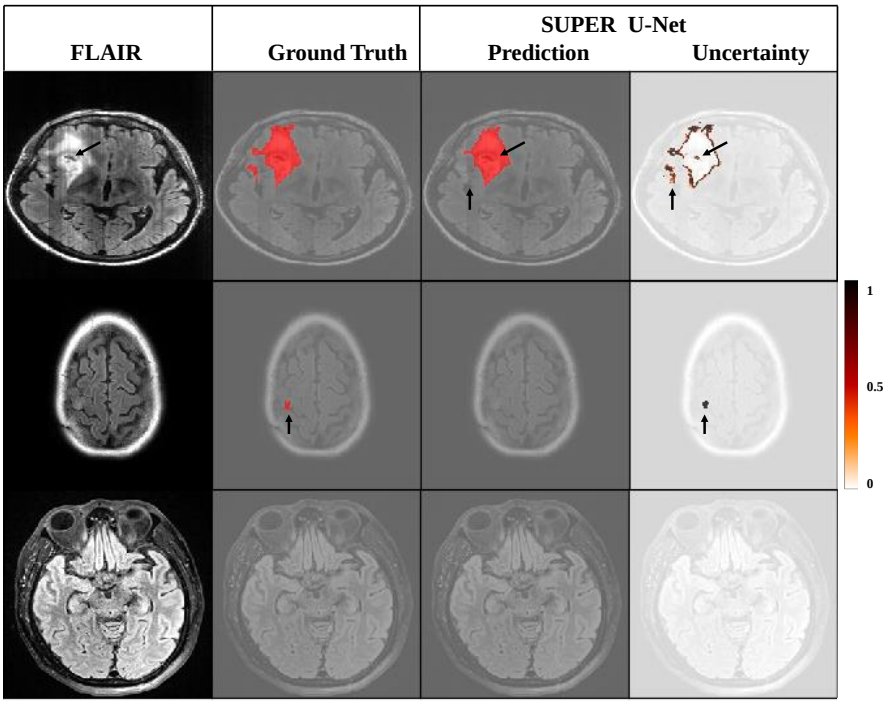


Fig. 6. Sample scans from the clinical data. Images show (left to right) the Flair input image, the ground-truth segmentation, the SUPER U-Net prediction and the uncertainty map overlaid on the input scan. The black arrows point to regions incorrectly classified by the network or unusually low (atypical) signal in the FLAIR.

TABLE VII
DSC FOR TEST SAMPLE FROM BRATS DATA - PERFORMANCE COMPARISON BEFORE AND AFTER REMOVAL OF UNCERTAIN PIXELS.

	Whole			*Core*			*Enhancing*		
	Bayes U-Net	**Ensemble U-Net**	**SUPER U-net**	**Bayes U-Net**	**Ensemble U-Net**	**SUPER U-net**	**Bayes U-Net**	**Ensemble U-Net**	**SUPER U-net**
Noise Free									
Original	.96	.96	.97	.85	.87	.89	.97	.96	.98
Uncertain Pixels Removed	.99 ↑	.99 ↑	1 ↑	.91 ↑	.88 ↑	.90 ↑	1 ↑	.98 ↑	1 ↑
Gaussian Noise added to entire input (SNR $\approx$ 20)									
Original	.56	.14	.97	.40	.16	.86	.58	.3	.86
Uncertain Pixels Removed	.11↓	0 ↓	.98 ↑	.40	.10↓	.99 ↑	.61 ↑	.21 ↓	1 ↑
Untargeted adversarial attacks (SNR $\approx$ 12)									
Original	.90	.91	.94	.74	.81	.78	.89	.91	.95
Uncertain Pixels Removed	.88 ↓	.79 ↓	.95 ↑	.75 ↑	.89 ↑	.81 ↑	1 ↑	.90 ↓	1 ↑
Targeted adversarial attacks (SNR $\approx$ 18): source 3, target 2									
Original	.93	.98	.99	.89	.90	.89	.95	.96	.97
Uncertain Pixels Removed	.90 ↓	.98	.99	.96 ↑	.96 ↑	.95 ↑	1 ↑	.98 ↑	1 ↑

TABLE VIII
SUPER U-NET PREDICTIVE VARIANCE FOR BRATS DATASET.

	Whole	**Core**	**Enhancing**
Correct	.007	.008	.008
Incorrect	.289	.307	.336

prompts the physicians to false negative, i.e., missed tumor region, and an unusual low SNR region inside the tumor structure. The uncertainty map can prompt the physician to pay particular attention to regions of low confidence rather than reviewing the model's prediction as a whole. ML systems that do not involve a physician-in-the-loop can flag the scan and request human intervention when uncertainty is above a set threshold.

3) Inference Time: We report the average inference time of all four networks in Table IX. We note that SUPER U-Net requires almost twice the time to process a single image at inference time compared to the deterministic U-Net. The increased processing time is related to the propagation of the covariance information that requires performing additional operations. The other approaches that deliver uncertainty, namely Bayes U-Net and Ensemble U-Net, take the same time as that of a deterministic U-Net for one pass (or one model). However, these approaches will need multiple passes to calculate the variance of the prediction. For example, we used $N = 20$ for Bayes U-Net, which will lead to the inference time of 16.4 ms for each image, almost 8 times more than SUPER U-Net. Additionally, it is worth mentioning that ensemble approaches require an extended training time and additional storage as

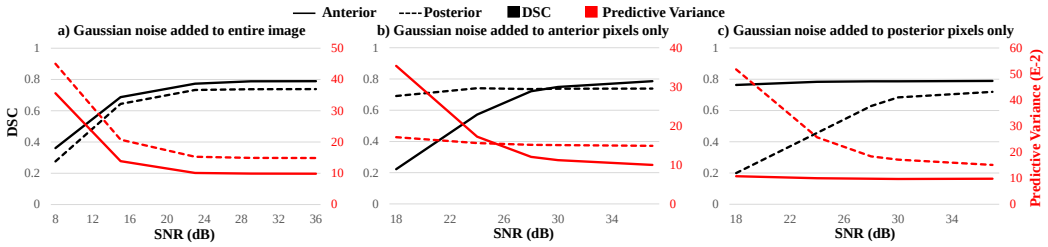


Fig. 7. Accuracy, measured by Dice Dimilarity Coefficient (DSC) and plotted in black, and average predictive variance of SUPER U-Net, plotted in red, under various levels of Gaussian noise added in the test data for hippocampus dataset. SNR denotes the Signal-to-Noise Ratio. (a) Noise added to the entire input. (b) Noise added to the anterior pixels only. (c) Noise added to the posterior pixels only.

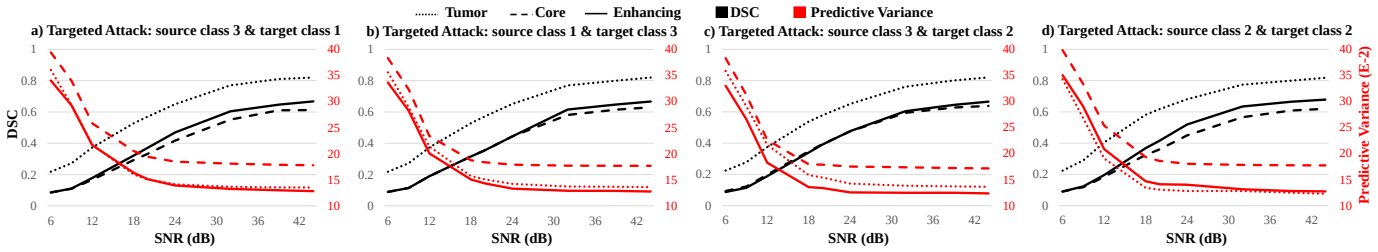


Fig. 8. Accuracy, measured by Dice Dimilarity Coefficient (DSCs) and plotted in black, and average predictive variance of SUPER U-Net, plotted in red, under various levels of adversarial attacks applied to the test data for BraTS dataset. SNR denotes the Signal-to-Noise Ratio. Test data is corrupted with targeted attacks: (a) source class 3 and target class 1, (b) source class 1 and target class 3, (c) source class 3 and target class 2, (d) source class 2 and target class 3.

TABLE IX
INFERENCE TIME PER IMAGE

	U-Net	Bayes U-Net	Ensemble U-Net	SUPER U-Net
Time (min)	0.81	0.82 N_1^*	0.81 N_2^*	1.92

$^*N_1$ is the number of runs through the network at inference time.
$^*N_2$ is the number of networks in the ensemble.

several models are trained and saved.

VI. Conclusion

We proposed a novel Bayesian framework, SUPER U-Net, to quantify intrinsic uncertainty in segmentation networks. The framework learns the first two moments, i.e., mean and covariance, of the posterior distribution of the model parameters through forward and backward propagation across all layers. We use first-order Taylor series approximation to analytically compute the moments at nonlinear layers. This is in contrast to MC approximation of the expected log-likelihood in other Bayesian approaches, which result in post-hoc estimation of the uncertainty. We targeted encoder-decoder architectures for medical image segmentation, i.e., notably those based on U-Net. At test time, the uncertainty in the decision is captured by the covariance matrix of the predictive distribution, which is available at the output of SUPER U-Net along with the prediction. The predictive covariance information is used to build uncertainty maps that provide crucial information about the network's confidence in the reliability of its prediction (i.e., segmentation). We have shown that areas incorrectly classified by our network are accompanied by higher uncertainty regions. Our results also demonstrate that SUPER U-Net model exhibits superior robustness to noise and adversarial attacks. Furthermore, the uncertainty maps offer a layer of transparency that draws the attention of supervising physicians to areas of low confidence. Nonetheless, clinical situations may arise where DL segmentation may not be under direct and continuous physician control; in such cases, it is important that the network recognizes high measures of uncertainty to generate an appropriate notification. Hence, our work paves the way for developing trustworthy and self-aware DL systems that can be safely deployed in mission-critical applications, notably healthcare.

Appendix A
Evaluation Under other Noise Types

To evaluate the robustness to noise, we include additional simulations with other noise types: Speckle, Salt and Pepper and Poisson noise. Tables X, XI, and XII report DSC values for U-Net, Bayes U-Net, Ensemble U-Net and SUPER U-Net under different levels of noise. For reference, we include also the noise-free case. In Fig. 9, we plot DSCs vs. SNR when Speckle noise is applied to the anterior (top plot) and posterior (bottom plot) structures of the Hippocampus test data. In Fig. 10, we plot DSCs vs. SNR for the three tumor regions. Each subplot compares the performance of the four networks for multiple levels of Speckle noise applied to the tumor structures of the Brats test set.

TABLE X
DSC FOR LUNGS DATASET - PERFORMANCE COMPARISON OF DIFFERENT NETWORKS UNDER SALT AND PEPPER NOISE.

	U-Net	Bayes U-Net	Ensemble U-Net	SUPER U-Net
Noise Free	**.83**	**.83**	**.83**	**.83**
Salt and Pepper noise added to the entire image				
SNR ≈ 22 dB	**.81**	.80	**.81**	.80
SNR ≈ 12 dB	.53	**.72**	.63	**.72**
SNR ≈ 7 dB	.26	.35	.20	**.52**
Salt and Pepper noise added to lung pixels only				
SNR ≈ 31 dB	**.83**	**.83**	**.83**	**.83**
SNR ≈ 21 dB	.55	.78	.63	**.79**
SNR ≈ 16 dB	.25	.35	.24	**.55**

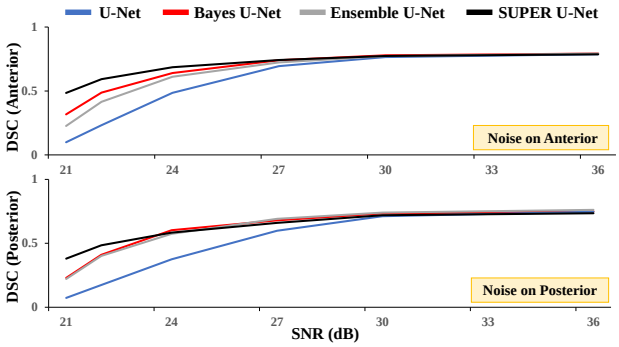


Fig. 9. Performance of four networks, i.e., U-Net (blue), Bayes U-Net (red), Ensemble U-Net (gray) and SUPER U-Net (black), under various levels of Speckle noise applied to the anterior (top) and Posterior (bottom) Hippocampus test data. We plot the DSC vs SNR (dB) for the 4 approaches. The y-axis displays the Dice Similarity Coefficient (DSC) at test time versus vs Signal to Noise Ratio (SNR), measured in dB.

In all noisy experiments, we note that SUPER U-Net is more robust to noise as compared to deterministic U-Net, Bayes U-Net, and Ensemble U-Net especially at low SNR values.

APPENDIX B
OVER AND UNDER SEGMENTATION EVALUATION

Under and over-segmentation are important considerations in medical AI applications that do not include a physician-in-the-loop approach. For example, under-segmentation of a tumor in radiation therapy planning is equivalent to under-treatment, which may lead to early tumor recurrence. On the other hand, over-segmentation of a brain tumor entails delivering harmful radiation to normal brain structures, which could affect cognitive behavior. Similarly, under and over-segmentation of longitudinal tumor volumes will lead to inaccurate diagnoses of growth and stability.

Our analysis includes a performance evaluation using over and under-segmentation. We report over-segmentation (O_s) and under-segmentation (U_s) rates. Both values range between 0 and 1 with lower values suggesting a better performance [72]. We compare the models with different levels of additive Gaussian noise (Tables XIII, XIV, XV) and adversarial attacks (Tables XVI, XVII, XVIII). We report in bold only methods that score best simultaneously in terms of O_s and U_s.

We note that there is no method that outperform the others on all datasets in terms of both O_s and U_s. As expected, there is a tradeoff between O_s and U_s, reducing the two scores

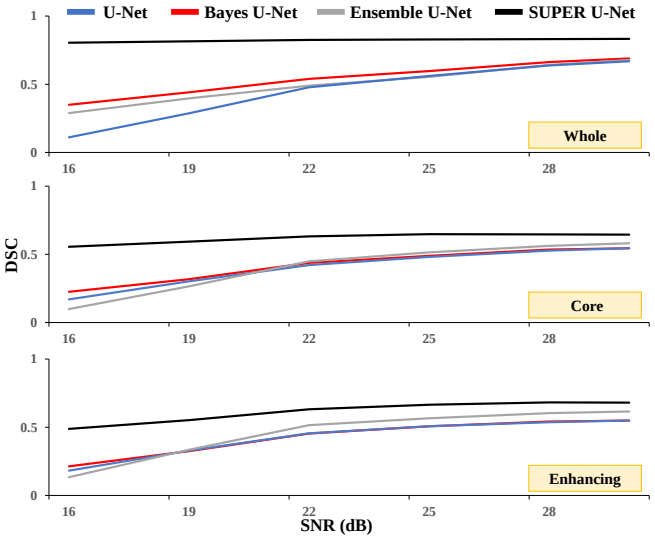


Fig. 10. Performance of the four networks, i.e., U-Net (blue), Bayes U-Net (red), Ensemble U-Net (gray) and SUPER U-Net (black), under various levels of Speckle noise added to the tumor structures of the BraTS test data. The three sub-plots show the Dice Similarity Coefficient (DSC) values for a range of Signal to Noise Ratios (SNRs) for three different tumor regions: whole tumor, core, and enhancing.

simultaneously is very challenging. We noted that some of the approaches tend to under-segment on average while others were either doing one or the other depending on the dataset or the noise/ attack level.

SUPER U-Net tends to find a fine balance between the two and does score the best in some tests. It is worth mentioning that comparing these results with the DSC values and inspecting the resulted segmented predictions, we noted that low O_s attained for higher noise levels were usually linked to networks under-segmenting entirely the structures of interest.

ACKNOWLEDGMENT

This work was supported by the National Science Foundation awards NSF ECCS-1903466 and NSF OAC-2008690. Giuseppina Carannante is supported by the US Department of Education through a Graduate Assistance in Areas of National Need (GAANN) program Award Number P200A180055. We are also grateful to UK EPSRC support through EP/T013265/1 project NSF-EPSRC: ShiRAS. Towards Safe and Reliable Autonomy in Sensor Driven Systems, and NJ Health Foundation support through Award number PC 78-21.

TABLE XI
DSC FOR HIPPOCAMPUS DATASET - PERFORMANCE COMPARISON UNDER SPECKLE AND POISSON NOISE.

	Anterior				**Posterior**			
	U-Net	**Bayes U-Net**	**Ensemble U-Net**	**SUPER U-Net**	**U-Net**	**Bayes U-Net**	**Ensemble U-Net**	**SUPER U-Net**
Noise Free	**.79**	**.79**	**.79**	**.79**	.76	.76	**.77**	.74
Speckle noise added to entire image								
SNR $\approx$ 20 dB	.77	.77	**.78**	**.78**	.73	.74	**.75**	.73
SNR $\approx$ 14 dB	.58	.65	.65	**.68**	.53	.54	.60	**.63**
SNR $\approx$ 10 dB	.18	.20	.23	**.48**	.09	.10	.12	**.37**
Poisson noise added to entire image								
SNR $\approx$ 20 dB	.74	.75	.75	**.77**	**.73**	.71	.72	.71
SNR $\approx$ 11 dB	.39	.38	.39	**.56**	.39	.38	.36	**.52**
SNR $\approx$ 8 dB	.22	.20	.22	**.40**	.23	.21	.21	**.36**

TABLE XII
DSC FOR BRATS DATASET - PERFORMANCE COMPARISON UNDER SPECKLE AND SALT AND PEPPER NOISE.

	Whole				***Core***				***Enhancing***			
	U-Net	**Bayes U-Net**	**Ensemble U-Net**	**SUPER U-net**	**U-Net**	**Bayes U-Net**	**Ensemble U-Net**	**SUPER U-net**	**U-Net**	**Bayes U-Net**	**Ensemble U-Net**	**SUPER U-net**
Noise free	.77	.77	.76	**.83**	.58	.58	.60	**.64**	.57	.57	.63	**.69**
Speckle noise added to tumor pixels only												
SNR $\approx$ 20 dB	.64	.63	.63	**.83**	.53	.53	.56	**.64**	.54	.54	.60	**.68**
SNR $\approx$ 14 dB	.46	.48	.46	**.81**	.42	.42	.44	**.64**	.45	.46	.51	**.65**
SNR $\approx$ 8 dB	.20	.26	.10	**.76**	.12	.13	.10	**.56**	.11	.14	.12	**.51**
Salt and Pepper noise added to tumor pixels only												
SNR $\approx$ 27 dB	.67	.67	.64	**.83**	.48	.48	.49	**.59**	.49	.48	.52	**.58**
SNR $\approx$ 24 dB	.58	.59	.55	**.83**	.42	.42	.43	**.58**	.42	.42	.46	**.54**
SNR $\approx$ 16 dB	.25	.28	.16	**.82**	.14	.17	.13	**.51**	.16	.14	.13	**.44**

TABLE XIII
OVER-SEGMENTATION AND UNDER-SEGMENTATION FOR LUNGS DATASET - PERFORMANCE COMPARISON UNDER ADDITIVE GAUSSIAN NOISE.

	U-Net	**Bayes U-Net**	**Ensemble U-Net**	**SUPER U-Net**
	O_s / U_s	O_s / U_s	O_s / U_s	O_s / U_s
Noise Free	.16 / .04	**.15 / .03**	.17 / .03	**.15 / .03**
Gaussian noise added to the entire image				
SNR $\approx$ 35 dB	.17 / .04	.16 / .04	.17 / .04	**.16 / .04**
SNR $\approx$ 3 dB	.84 / .04	.50 / .49	.64 / .35	.78 / .01
Gaussian noise added to lung pixels only				
SNR $\approx$ 31 dB	.16 / .02	**.15 / .04**	.16 / .03	**.15 / .04**
SNR $\approx$ 14 dB	.15 / .31	.15 / .84	.15 / .84	**.15 / .12**

TABLE XIV
OVER-SEGMENTATION AND UNDER-SEGMENTATION FOR HIPPOCAMPUS DATASET - PERFORMANCE COMPARISON UNDER ADDITIVE GAUSSIAN NOISE.

	Anterior				**Posterior**			
	U-Net	**Bayes U-Net**	**Ensemble U-Net**	**SUPER U-Net**	**U-Net**	**Bayes U-Net**	**Ensemble U-Net**	**SUPER U-Net**
	O_s / U_s	O_s / U_s	O_s / U_s	O_s / U_s	O_s / U_s	O_s / U_s	O_s / U_s	O_s / U_s
Noise free	.15 / .14	.13 / .17	.09 / .19	.15 / .15	.17 / .15	.15 / .19	.11 / .21	.14 / .23
Gaussian noise added to entire image								
SNR $\approx$ 23 dB	.14 / .18	.14 / .16	.09 / .19	.14 / .17	.17 / .17	.14 / .22	.11 / .21	.13 / .24
SNR $\approx$ 15 dB	.22 / .37	.12 / .39	.05 / .50	.15 / .30	.07 / .58	.15 / .39	.07 / .50	.11 / .40
SNR $\approx$ 8 dB	.22 / .71	.09 / .80	.02 / .90	.14 / .65	.01 / .94	.07 / .82	.02 / .89	.06 / .76
Gaussian noise added to Anterior pixels only								
SNR $\approx$ 30 dB	.13 / .29	.13 / .22	.08 / .30	.13 / .22	.16 / .16	.14 / .21	.10 / .23	.13 / .24
SNR $\approx$ 24 dB	.11 / .52	.10 / .67	.07 / .62	.13 / .42	.16 / .18	.13 / .25	.09 / .26	.13 / .25
SNR $\approx$ 18 dB	.08 / .90	.07 / .85	.06 / .90	.11 / .70	.14 / .25	.11 / .31	.08 / .34	.12 / .30
Gaussian noise added to Posterior pixels only								
SNR $\approx$ 30 dB	.15 / .16	.14 / .17	.09 / .20	.15 / .15	.14 / .26	.11 / .39	.09 / .34	.12 / .30
SNR $\approx$ 24 dB	.14 / .17	.13 / .18	.09 / .22	.14 / .16	.12 / .53	.07 / .77	.06 / .65	.10 / .54
SNR $\approx$ 18 dB	.13 / .22	.11 / .24	.07 / .26	.13 / .19	.09 / .82	.05 / .94	.04 / .92	.07 / .79

TABLE XV
OVER-SEGMENTATION AND UNDER-SEGMENTATION FOR BRATS DATASET - PERFORMANCE COMPARISON UNDER ADDITIVE GAUSSIAN NOISE.

	Whole				***Core***				***Enhancing***			
	U-Net	**Bayes U-Net**	**Ensemble U-Net**	**SUPER U-Net**	**U-Net**	**Bayes U-Net**	**Ensemble U-Net**	**SUPER U-Net**	**U-Net**	**Bayes U-Net**	**Ensemble U-Net**	**SUPER U-Net**
	O_s / U_s	O_s / U_s	O_s / U_s	O_s / U_s	O_s / U_s	O_s / U_s	O_s / U_s	O_s / U_s	O_s / U_s	O_s / U_s	O_s / U_s	O_s / U_s
Noise free	.11 / .22	.11 / .21	.06 / .27	.10 / .14	.29 / .21	.24 / .26	.14 / .34	.08 / .34	.41 / .11	.40 / .12	.29 / .16	.25 /.15
Gaussian noise added to entire image												
SNR $\approx$ 24 dB	.10 / .25	.10 / .26	.06 / .31	.09 / .14	.29 / .22	.25 / .27	.14 / .35	.08 / .35	.40 / .12	.39 / .13	.29 / .17	.25 / .15
SNR $\approx$ 18 dB	.08 / .31	.07 / .33	.04 / .37	.09 / .15	.30 / .24	.24 / .30	.14 / .37	.08 / .36	.39 / .15	.37 / .16	.27 / .20	.26 / .15
SNR $\approx$ 9 dB	.13 / .48	.08 / .55	.02 / .64	.09 / .19	.36 / .37	.29 / .42	.16 / .57	.16 / .32	.39 / .31	.38 / .33	.18 / .46	.30 / .15
Gaussian noise added to tumor pixels only												
SNR $\approx$ 32 dB	.10 / .29	.09 / .30	.06 / .35	.10 / .14	.31 / .22	.26 / .28	.15 / .35	.09 / .35	.40 / .14	.39 / .15	.29 / .19	**.26 / .14**
SNR $\approx$ 25 dB	.08 / .39	.08 / .42	.05 / .47	.10 / .14	.31 / .29	.26 / .35	.17 / .41	.13 / .31	.39 / .20	.37 / .23	.28 / .26	**.28 / .14**
SNR $\approx$ 13 dB	.06 / .80	.05 / .86	.02 / .95	.13 / .16	.27 / .65	.19 / .78	.05 / .93	.10 / .53	.32 / .61	.25 / .72	.08 / .90	.48 / .09

TABLE XVI
DSC FOR LUNGS DATASET - PERFORMANCE COMPARISON UNDER UNTARGETED ADVERSARIAL ATTACKS.

	U-Net	**Bayes U-Net**	**Ensemble U-Net**	**SUPER U-Net**
	O_s / U_s	O_s / U_s	O_s / U_s	O_s / U_s
Noise Free	.16 / .04	**.15 / .03**	.17 / .03	**.15 / .03**
Untargeted attacks generated using FGSM				
SNR $\approx$ 55 dB	.19 / .03	.17 / .03	.18 / .04	.16 / .05
SNR $\approx$ 29 dB	.48 / .04	.41 / .05	.51 / .02	.39 / .06
SNR $\approx$ 10 dB	.85 / .01	.80 / .05	.79 / .08	.65 / .06

TABLE XVII
OVER-SEGMENTATION AND UNDER-SEGMENTATION FOR HIPPOCAMPUS DATASET - PERFORMANCE COMPARISON UNDER VARIOUS LEVELS OF TARGETED ADVERSARIAL ATTACKS.

	Anterior				***Posterior***			
	U-Net	**Bayes U-Net**	**Ensemble U-Net**	**SUPER U-Net**	**U-Net**	**Bayes U-Net**	**Ensemble U-Net**	**SUPER U-Net**
	O_s / U_s	O_s / U_s	O_s / U_s	O_s / U_s	O_s / U_s	O_s / U_s	O_s / U_s	O_s / U_s
Noise Free	.15 / .14	.13 / .17	.09 / .19	.15 / .15	.17 / .15	.15 / .19	.11 / .21	.14 / .23
Targeted adversarial attacks - source: label 1, target: label 2								
SNR $\approx$ 29 dB	.26 / .08	.23 / .09	.13 / .16	.25 / .09	.23 / .25	.19 / .31	.12 / .26	.17 / .29
SNR $\approx$ 23 dB	.27 / .09	.27 / .09	.14 / .18	.26 / .10	.24 / .31	.18 / .40	.12 / .36	.16 / .35
SNR $\approx$ 15 dB	.23 / .39	.35 / .27	.10 / .51	.27 / .30	.16 / .64	.08 / .78	.07 / .75	.11 / .62
Targeted adversarial attacks - source: label 2, target: label 1								
SNR $\approx$ 29 dB	.19 / .25	.17 / .24	.12 / .24	.17 / .23	.31 / .08	.27 / .11	.15 / .19	.24 / .16
SNR $\approx$ 23 dB	.19 / .31	.19 / .26	.10 / .29	.18 / .27	.33 / .09	.27 / .12	.16 / .20	.25 / .17
SNR $\approx$ 15 dB	.16 / .60	.30 / .44	.06 / .65	.19 / .27	.22 / .41	.13 / .54	.09 / .54	.26 / .17

TABLE XVIII
OVER-SEGMENTATION AND UNDER-SEGMENTATION FOR BRATS DATASET - PERFORMANCE COMPARISON UNDER VARIOUS LEVELS OF UNTARGETED AND TARGETED ADVERSARIAL ATTACKS.

	Whole				***Core***				***Enhancing***			
	U-Net	**Bayes U-Net**	**Ensemble U-Net**	**SUPER U-Net**	**U-Net**	**Bayes U-Net**	**Ensemble U-Net**	**SUPER U-Net**	**U-Net**	**Bayes U-Net**	**Ensemble U-Net**	**SUPER U-Net**
	O_s / U_s	O_s / U_s	O_s / U_s	O_s / U_s	O_s / U_s	O_s / U_s	O_s / U_s	O_s / U_s	O_s / U_s	O_s / U_s	O_s / U_s	O_s / U_s
Noise free	.11 / .22	.11 / .21	.06 / .27	.10 / .14	.29 / .21	.24 / .26	.14 / .34	.08 / .34	.41 / .11	.40 / .12	.29 / .16	.25 /.15
Untargeted attacks generated using FGSM												
SNR $\approx$ 39 dB	.23 / .23	.18 / .24	.08 / .31	.15 / .12	.48 / .17	.39 / .23	.18 / .35	13 / .33	.55 / .11	.49 / .12	.32 / .19	.30 / .12
SNR $\approx$ 12 dB	.28 / .47	.32 / .39	.07 / .66	.33 / .20	.53 / .32	.58 / .26	.30 / .52	.48 / .27	.56 / .30	.62 / .22	.39 / .43	.58 / .20
Targeted adversarial attacks - source: label 3, target: label 1												
SNR $\approx$ 44 dB	.16 / .23	.15 / .24	.07 / .29	.12 / .14	.39 / .20	.33 / .25	.15 / .35	.09 / .35	.47 / .11	.45 / .13	.30 / .17	.25 / .17
SNR $\approx$ 19 dB	.27 / .43	.24 / .47	.06 / .52	.23 / .32	.50 / .31	.46 / .35	.20 / .51	.24 / .47	.51 / .28	.53 / .27	.28 / .39	.30 / .34
Targeted adversarial attacks - source: label 1, target: label 3												
SNR $\approx$ 44 dB	.16 / .23	.15 / .24	.07 / .29	.12 / .13	.39/ .19	.34 / .24	.16 / .34	.10 / .35	.48 / .11	.45 / .13	.30 / .17	.27 / .15
SNR $\approx$ 19 dB	.27 / .44	.24 / .46	.06 / .52	.24 / .31	.51 / .31	.47 / .34	.20 / .47	.20 / .47	.51 / .29	.53 / .26	.35 / .36	.29 / .34
Targeted adversarial attacks - source: label 3, target: label 2												
SNR $\approx$ 44 dB	.16 / .23	.15 / .23	.07 / .29	.13 / .13	.40 / .16	.34 / .22	.16 / .33	.11 / .34	.49 / .10	.46 / .12	.31 / .16	.28 / .14
SNR $\approx$ 19 dB	.28 / .43	.24 / .46	.06 / .52	.24 / .30	.52 / .28	.48 / .31	.21 / .45	.25 / .40	.53 / .25	.55 / .25	.30 / .32	.39 / .29
Targeted adversarial attacks - source: label 2, target: label 3												
SNR $\approx$ 44 dB	.15 / .23	.14 / .24	.07 / .29	.11 / .14	.32 / .23	.27 / .29	.13 / .36	.70 / .39	.43 / .13	.41 / .14	.28 / .18	.23 / .18
SNR $\approx$ 19 dB	.26 / .45	.22 / .49	.05 / .55	.22 / .27	.45 / .36	.30 / .39	.14 / .52	.19 / .54	.46 / .32	.48 / .30	.21 / .39	.28 / .40

REFERENCES

[1] M. L. Giger, "Machine learning in medical imaging," *Journal of the American College of Radiology*, vol. 15, no. 3, pp. 512–520, 2018.

[2] D. S. Ting, Y. Liu, P. Burlina, X. Xu, N. M. Bressler, and T. Y. Wong, "Ai for medical imaging goes deep," *Nature medicine*, vol. 24, no. 5, pp. 539–540, 2018.

[3] X. Liu, L. Faes, A. U. Kale, S. K. Wagner, D. J. Fu, A. Bruynseels, T. Mahendiran, G. Moraes, M. Shamdas, C. Kern *et al.*, "A comparison of deep learning performance against health-care professionals in detecting diseases from medical imaging: a systematic review and meta-analysis," *The lancet digital health*, vol. 1, no. 6, pp. e271–e297, 2019.

[4] A. Esteva, B. Kuprel, R. A. Novoa, J. Ko, S. M. Swetter, H. M. Blau, and S. Thrun, "Dermatologist-level classification of skin cancer with deep neural networks," *nature*, vol. 542, no. 7639, pp. 115–118, 2017.

[5] C. Guo, G. Pleiss, Y. Sun, and K. Q. Weinberger, "On calibration of modern neural networks," in *International Conference on Machine Learning*. PMLR, 2017, pp. 1321–1330.

[6] B. Biggio and F. Roli, "Wild patterns: Ten years after the rise of adversarial machine learning," *Pattern Recognition*, vol. 84, pp. 317–331, 2018.

[7] I. J. Goodfellow, J. Shlens, and C. Szegedy, "Explaining and harnessing adversarial examples," *arXiv preprint arXiv:1412.6572*, 2014.

[8] H. Hirano, A. Minagi, and K. Takemoto, "Universal adversarial attacks on deep neural networks for medical image classification," *BMC medical imaging*, vol. 21, no. 1, pp. 1–13, 2021.

[9] S. G. Finlayson, J. D. Bowers, J. Ito, J. L. Zittrain, A. L. Beam, and I. S. Kohane, "Adversarial attacks on medical machine learning," *Science*, vol. 363, no. 6433, pp. 1287–1289, 2019.

[10] Y. Gal and Z. Ghahramani, "Dropout as a Bayesian Approximation: Representing Model Uncertainty in Deep Learning," in *international conference on machine learning*, 2016, pp. 1050–1059.

[11] B. Lakshminarayanan, A. Pritzel, and C. Blundell, "Simple and Scalable Predictive Uncertainty Estimation using Deep Ensembles," in *Advances in neural information processing systems*, 2017, pp. 6402–6413.

[12] X. Lu and B. Van Roy, "Ensemble Sampling," in *Advances in neural information processing systems*, 2017, pp. 3258–3266.

[13] A. Graves, "Practical Variational Inference for Neural Networks," in *Advances in neural information processing systems*, 2011, pp. 2348–2356.

[14] D. Dera, N. C. Bouaynaya, G. Rasool, R. Shterenberg, and H. M. Fathallah-Shaykh, "Premium-cnn: Propagating uncertainty towards robust convolutional neural networks," *IEEE Transactions on Signal Processing*, vol. 69, pp. 4669–4684, 2021.

[15] G. Carannante, D. Dera, G. Rasool, N. Bouaynaya, and L. Mihaylova, "Robust Learning via Ensemble Density Propagation in Deep Neural Networks," in *IEEE International Workshop on Machine Learning for Signal Processing*. Sheffield, 2020.

[16] G. Carannante, N. C. Bouaynaya, and L. Mihaylova, "An enhanced particle filter for uncertainty quantification in neural networks," in *2021 IEEE 24th International Conference on Information Fusion (FUSION)*. IEEE, 2021, pp. 1–7.

[17] E. Goan and C. Fookes, "Bayesian neural networks: An introduction and survey," in *Case Studies in Applied Bayesian Data Science*. Springer, 2020, pp. 45–87.

[18] A. Doucet, A. M. Johansen *et al.*, "A tutorial on particle filtering and smoothing: Fifteen years later."

[19] N. Amor, G. Rasool, and N. C. Bouaynaya, "Constrained state estimation-a review," *arXiv preprint arXiv:1807.03463*, 2018.

[20] S. Minaee, Y. Y. Boykov, F. Porikli, A. J. Plaza, N. Kehtarnavaz, and D. Terzopoulos, "Image segmentation using deep learning: A survey," *IEEE Transactions on Pattern Analysis and Machine Intelligence*, 2021.

[21] J. Long, E. Shelhamer, and T. Darrell, "Fully convolutional networks for semantic segmentation," in *Proceedings of the IEEE conference on computer vision and pattern recognition*, 2015, pp. 3431–3440.

[22] M. Drozdzal, E. Vorontsov, G. Chartrand, S. Kadoury, and C. Pal, "The importance of skip connections in biomedical image segmentation," in *Deep learning and data labeling for medical applications*. Springer, 2016, pp. 179–187.

[23] L.-C. Chen, G. Papandreou, I. Kokkinos, K. Murphy, and A. L. Yuille, "Deeplab: Semantic image segmentation with deep convolutional nets, atrous convolution, and fully connected crfs," *IEEE transactions on pattern analysis and machine intelligence*, vol. 40, no. 4, pp. 834–848, 2017.

[24] V. Badrinarayanan, A. Kendall, and R. Cipolla, "Segnet: A deep convolutional encoder-decoder architecture for image segmentation," *IEEE transactions on pattern analysis and machine intelligence*, vol. 39, no. 12, pp. 2481–2495, 2017.

[25] S. Jégou, M. Drozdzal, D. Vazquez, A. Romero, and Y. Bengio, "The one hundred layers tiramisu: Fully convolutional densenets for semantic segmentation," in *Proceedings of the IEEE conference on computer vision and pattern recognition workshops*, 2017, pp. 11–19.

[26] K. He, X. Zhang, S. Ren, and J. Sun, "Deep residual learning for image recognition," in *Proceedings of the IEEE conference on computer vision and pattern recognition*, 2016, pp. 770–778.

[27] G. Huang, Z. Liu, L. Van Der Maaten, and K. Q. Weinberger, "Densely connected convolutional networks," in *Proceedings of the IEEE conference on computer vision and pattern recognition*, 2017, pp. 4700–4708.

[28] O. Ronneberger, P. Fischer, and T. Brox, "U-net: Convolutional networks for biomedical image segmentation," in *International Conference on Medical image computing and computer-assisted intervention*. Springer, 2015, pp. 234–241.

[29] D. E. Cahall, G. Rasool, N. C. Bouaynaya, and H. M. Fathallah-Shaykh, "Inception modules enhance brain tumor segmentation," *Frontiers in computational neuroscience*, vol. 13, p. 44, 2019.

[30] S.-T. Tran, C.-H. Cheng, T.-T. Nguyen, M.-H. Le, and D.-G. Liu, "Tmd-unet: Triple-unet with multi-scale input features and dense skip connection for medical image segmentation," in *Healthcare*, vol. 9, no. 1. Multidisciplinary Digital Publishing Institute, 2021, p. 54.

[31] M. U. Rehman, S. Cho, J. H. Kim, and K. T. Chong, "Bu-net: Brain tumor segmentation using modified u-net architecture," *Electronics*, vol. 9, no. 12, p. 2203, 2020.

[32] X. Li, W. Qian, D. Xu, and C. Liu, "Image segmentation based on improved unet," in *Journal of Physics: Conference Series*, vol. 1815, no. 1. IOP Publishing, 2021, p. 012018.

[33] A. Kendall, V. Badrinarayanan, and R. Cipolla, "Bayesian segnet: Model uncertainty in deep convolutional encoder-decoder architectures for scene understanding," *arXiv preprint arXiv:1511.02680*, 2015.

[34] A. G. Roy, S. Conjeti, N. Navab, C. Wachinger, A. D. N. Initiative *et al.*, "Bayesian quicknat: Model uncertainty in deep whole-brain segmentation for structure-wise quality control," *NeuroImage*, vol. 195, pp. 11–22, 2019.

[35] T. Nair, D. Precup, D. L. Arnold, and T. Arbel, "Exploring uncertainty measures in deep networks for multiple sclerosis lesion detection and segmentation," *Medical image analysis*, vol. 59, p. 101557, 2020.

[36] Y. Kwon, J.-H. Won, B. J. Kim, and M. C. Paik, "Uncertainty quantification using bayesian neural networks in classification: Application to biomedical image segmentation," *Computational Statistics & Data Analysis*, vol. 142, p. 106816, 2020.

[37] A. Jungo, R. McKinley, R. Meier, U. Knecht, L. Vera, J. Pérez-Beteta, D. Molina-García, V. M. Pérez-García, R. Wiest, and M. Reyes, "Towards Uncertainty-Assisted Brain Tumor Segmentation and Survival Prediction," in *International MICCAI Brainlesion Workshop*. Springer, 2017, pp. 474–485.

[38] K. Kamnitsas, W. Bai, E. Ferrante, S. McDonagh, M. Sinclair, N. Pawlowski, M. Rajchl, M. Lee, B. Kainz, D. Rueckert *et al.*, "Ensembles of multiple models and architectures for robust brain tumour segmentation," in *International MICCAI brainlesion workshop*. Springer, 2017, pp. 450–462.

[39] X. Feng, N. J. Tustison, S. H. Patel, and C. H. Meyer, "Brain tumor segmentation using an ensemble of 3d u-nets and overall survival prediction using radiomic features," *Frontiers in computational neuroscience*, vol. 14, p. 25, 2020.

[40] A. J. Larrazabal, C. Martínez, J. Dolz, and E. Ferrante, "Orthogonal ensemble networks for biomedical image segmentation," in *International Conference on Medical Image Computing and Computer-Assisted Intervention*. Springer, 2021, pp. 594–603.

[41] M. G. B. Calisto and S. K. Lai-Yuen, "Self-adaptive 2d-3d ensemble of fully convolutional networks for medical image segmentation," in *Medical Imaging 2020: Image Processing*, vol. 11313. International Society for Optics and Photonics, 2020, p. 113131W.

[42] C. F. Baumgartner, K. C. Tezcan, K. Chaitanya, A. M. Hötker, U. J. Muehlematter, K. Schawkat, A. S. Becker, O. Donati, and E. Konukoglu, "Phiseg: Capturing uncertainty in medical image segmentation," in *International Conference on Medical Image Computing and Computer-Assisted Intervention*. Springer, 2019, pp. 119–127.

[43] G. Wang, W. Li, S. Ourselin, and T. Vercauteren, "Automatic brain tumor segmentation based on cascaded convolutional neural networks with uncertainty estimation," *Frontiers in computational neuroscience*, vol. 13, p. 56, 2019.

[44] B. Lambert, F. Forbes, S. Doyle, A. Tucholka, and M. Dojat, "Fast uncertainty quantification for deep learning-based mr brain segmenta-

tion," in *Conference francophone pour l'extraction et la gestion des connaissances*, 2022.
[45] K. Hoebel, V. Andrearczyk, A. Beers, J. Patel, K. Chang, A. Depeursinge, H. Müller, and J. Kalpathy-Cramer, "An exploration of uncertainty information for segmentation quality assessment," in *Medical Imaging 2020: Image Processing*, vol. 11313. International Society for Optics and Photonics, 2020, p. 113131K.
[46] H. Asgharnezhad, A. Shamsi, R. Alizadehsani, A. Khosravi, S. Nahavandi, Z. A. Sani, D. Srinivasan, and S. M. S. Islam, "Objective evaluation of deep uncertainty predictions for covid-19 detection," *Scientific Reports*, vol. 12, no. 1, pp. 1–11, 2022.
[47] B. Lakshminarayanan, A. Pritzel, and C. Blundell, "Simple and scalable predictive uncertainty estimation using deep ensembles," *arXiv preprint arXiv:1612.01474*, 2016.
[48] B. Ghoshal, A. Tucker, B. Sanghera, and W. Lup Wong, "Estimating uncertainty in deep learning for reporting confidence to clinicians in medical image segmentation and diseases detection," *Computational Intelligence*, vol. 37, no. 2, pp. 701–734, 2021.
[49] G. E. Hinton and D. Van Camp, "Keeping the neural networks simple by minimizing the description length of the weights," in *Proceedings of the sixth annual conference on Computational learning theory*, 1993, pp. 5–13.
[50] C. Blundell, J. Cornebise, K. Kavukcuoglu, and D. Wierstra, "Weight Uncertainty in Neural Networks," *arXiv preprint arXiv:1505.05424*, 2015.
[51] M. Jun, G. Cheng, W. Yixin, A. Xingle, G. Jiantao, Y. Ziqi, Z. Minqing, L. Xin, D. Xueyuan, C. Shucheng, W. Hao, M. Sen, Y. Xiaoyu, N. Ziwei, L. Chen, T. Lu, Z. Yuntao, Z. Qiongjie, D. Guoqiang, and H. Jian, "COVID-19 CT Lung and Infection Segmentation Dataset," Apr. 2020. [Online]. Available: https://doi.org/10.5281/zenodo.3757476
[52] A. L. Simpson, M. Antonelli, S. Bakas, M. Bilello, K. Farahani, B. Van Ginneken, A. Kopp-Schneider, B. A. Landman, G. Litjens, B. Menze *et al.*, "A large annotated medical image dataset for the development and evaluation of segmentation algorithms," *arXiv preprint arXiv:1902.09063*, 2019.
[53] B. H. Menze, A. Jakab, S. Bauer, J. Kalpathy-Cramer, K. Farahani, J. Kirby, Y. Burren, N. Porz, J. Slotboom, R. Wiest *et al.*, "The multimodal brain tumor image segmentation benchmark (brats)," *IEEE transactions on medical imaging*, vol. 34, no. 10, pp. 1993–2024, 2014.
[54] H. M. Fathallah-Shaykh, A. DeAtkine, E. Coffee, E. Khayat, A. K. Bag, X. Han, P. P. Warren, M. Bredel, J. Fiveash, J. Markert, N. Bouaynaya, and L. B. Nabors, "Diagnosing growth in low-grade gliomas with and without longitudinal volume measurements: A retrospective observational study," *PLoS Med*, vol. 16, no. 5, p. e1002810, 05 2019.
[55] S. Jadon, "A survey of loss functions for semantic segmentation," in *2020 IEEE Conference on Computational Intelligence in Bioinformatics and Computational Biology (CIBCB)*. IEEE, 2020, pp. 1–7.
[56] A. Mehrtash, W. M. Wells, C. M. Tempany, P. Abolmaesumi, and T. Kapur, "Confidence calibration and predictive uncertainty estimation for deep medical image segmentation," *IEEE transactions on medical imaging*, vol. 39, no. 12, pp. 3868–3878, 2020.
[57] J. Sander, B. D. de Vos, J. M. Wolterink, and I. Išgum, "Towards increased trustworthiness of deep learning segmentation methods on cardiac mri," in *Medical imaging 2019: image Processing*, vol. 10949. SPIE, 2019, pp. 324–330.
[58] Y. Liu, X. Chen, C. Liu, and D. Song, "Delving into transferable adversarial examples and black-box attacks," *arXiv preprint arXiv:1611.02770*, 2016.
[59] A. Madry, A. Makelov, L. Schmidt, D. Tsipras, and A. Vladu, "Towards deep learning models resistant to adversarial attacks," *arXiv preprint arXiv:1706.06083*, 2017.
[60] B. McCrindle, K. Zukotynski, T. E. Doyle, and M. D. Noseworthy, "A radiology-focused review of predictive uncertainty for ai interpretability in computer-assisted segmentation," *Radiology: Artificial Intelligence*, vol. 3, no. 6, 2021.
[61] R. Mehta, A. Filos, Y. Gal, and T. Arbel, "Uncertainty evaluation metric for brain tumour segmentation," *arXiv preprint arXiv:2005.14262*, 2020.
[62] Z. Chang, "Will ai improve tumor delineation accuracy for radiation therapy?" 2019.
[63] B. E. Nelms, W. A. Tomé, G. Robinson, and J. Wheeler, "Variations in the contouring of organs at risk: test case from a patient with oropharyngeal cancer," *International Journal of Radiation Oncology* Biology* Physics*, vol. 82, no. 1, pp. 368–378, 2012.
[64] H. Sandström, H. Jokura, C. Chung, and I. Toma-Dasu, "Multi-institutional study of the variability in target delineation for six targets commonly treated with radiosurgery," *Acta Oncologica*, vol. 57, no. 11, pp. 1515–1520, 2018.
[65] G. P. Mazzara, R. P. Velthuizen, J. L. Pearlman, H. M. Greenberg, and H. Wagner, "Brain tumor target volume determination for radiation treatment planning through automated mri segmentation," *International Journal of Radiation Oncology* Biology* Physics*, vol. 59, no. 1, pp. 300–312, 2004.
[66] C. F. Njeh, L. Dong, and C. G. Orton, "Igrt has limited clinical value due to lack of accurate tumor delineation," *Medical Physics*, vol. 40, no. 4, p. 040601, 2013.
[67] S. K. Vinod, M. Min, M. G. Jameson, and L. C. Holloway, "A review of interventions to reduce inter-observer variability in volume delineation in radiation oncology," *Journal of medical imaging and radiation oncology*, vol. 60, no. 3, pp. 393–406, 2016.
[68] K. Kim, M. Chun, H. Jin, W. Jung, K. H. Shin, S. S. Shin, Y. J. Kim, S.-H. Park, J. H. Kim, Y. H. Kim *et al.*, "Inter-institutional variation in intensity-modulated radiotherapy for breast cancer in korea (krog 19-01)," *Anticancer Research*, vol. 41, no. 6, pp. 3145–3152, 2021.
[69] M. Pavic, M. Bogowicz, X. Würms, S. Glatz, T. Finazzi, O. Riesterer, J. Roesch, L. Rudofsky, M. Friess, P. Veit-Haibach *et al.*, "Influence of inter-observer delineation variability on radiomics stability in different tumor sites," *Acta Oncologica*, vol. 57, no. 8, pp. 1070–1074, 2018.
[70] J. van der Veen, A. Gulyban, and S. Nuyts, "Interobserver variability in delineation of target volumes in head and neck cancer," *Radiotherapy and Oncology*, vol. 137, pp. 9–15, 2019.
[71] C. W. Wee, W. Sung, H.-C. Kang, K. H. Cho, T. J. Han, B.-K. Jeong, J.-U. Jeong, H. Kim, I. A. Kim, J. H. Kim *et al.*, "Evaluation of variability in target volume delineation for newly diagnosed glioblastoma: a multi-institutional study from the korean radiation oncology group," *Radiation Oncology*, vol. 10, no. 1, pp. 1–9, 2016.
[72] L. Mou, Y. Zhao, H. Fu, Y. Liu, J. Cheng, Y. Zheng, P. Su, J. Yang, L. Chen, A. F. Frangi *et al.*, "Cs2-net: Deep learning segmentation of curvilinear structures in medical imaging," *Medical image analysis*, vol. 67, p. 101874, 2021.